Design and Analysis of Plasmonic Couplers with Enhanced Performance

by

Md Saiful Islam Sumon

MASTER OF SCIENCE
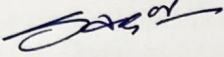**IN**
ELECTRICAL AND ELECTRONIC ENGINEERING

Department of Electrical and Electronic Engineering
Islamic University of Technology (IUT)
Board Bazar, Gazipur-1704, Bangladesh.
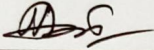September, 2021.

CERTIFICATE OF APPROVAL

The thesis titled,"**Design and Analysis of Plasmonic Couplers with Enhanced Performance** " submitted by Md Saiful Islam Sumon, St. No. 181021016 of Academic Year 2018-19 has been found as satisfactory and accepted as partial fulfillment of the requirement for the Degree MASTER OF SCIENCE IN ELECTRICAL AND ELECTRONIC ENGINEERING on September 23, 2021.

Board of Examiners:

Dr. Rakibul Hasan Sagor (Supervisor)
Associate Professor,   Chairman
Electrical and Electronic Engineering Department,
Islamic University of Technology (IUT), Gazipur.

Dr. Md. Ruhul Amin (Ex-Officio)
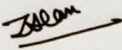Professor and Head,   Member
Electrical and Electronic Engineering Department,
Islamic University of Technology (IUT), Gazipur.

Dr. Mohammad Rakibul Islam
Professor,   Member
Electrical and Electronic Engineering Department,
Islamic University of Technology (IUT), Gazipur.

Dr. Mohammad Jahangir Alam
Professor,   Member (External)
Electrical and Electronic Engineering Department,
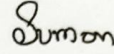Bangladesh University of Engineering and Technology (BUET), Dhaka.

Declaration of Candidate

It is hereby declared that this thesis report or any part of it has not been submitted elsewhere for the award of any Degree or Diploma.

Dr. Rakibul Hasan Sagor
Associate Professor,
Electrical and Electronic Engineering department,
Islamic University of Technology (IUT),
Date: September 23, 2021.

Md Saiful Islam Sumon
Student No.: 181021016,
Academic Year: 2018-19,
Date: September 23, 2021.

Dedicated to my family members.

Table of Contents

List of Figures

List of Tables

List of Abbreviations

CPP	Channel Plasmon Polariton
CVD	Chemical vapor deposition
CST	Computer Simulation Technology
DMD	Dielectric-Metal-Mielectric
EM	Electromagnetic
EMF	Electromotive Force
FDTD	Finite Difference Time Domain
FIT	Finite Integration Technique
MDM	Metal-Dielectric-Metal
PVD	Physical Vapor Deposition
SPP	Surface Plasmon Polariton
TE	Transverse Electric
TM	Transverse Magnetic
VSWR	Voltage Standing Wave Ratio

Acknowledgment

At first, I would like to thank Almighty Allah (SWT), who is in control of everything for helping me in every aspect of my life.

I would also like to express my sincere gratitude to my thesis supervisor Dr. Rakibul Hasan Sagor, Associate professor, Department of Electrical and Electronic Engineering, Islamic University of Technology (IUT), for his continuous support and motivation to my research work, study as well as personal life.

I am also thankful to the electrical and electronic engineering department of Islamic University of Technology (IUT) for supporting me both in course and thesis works.

Finally, I would like to thank my family members for their patience and help throughout my life.

Md Saiful Islam Sumon
September, 2021

Abstract

The capability of plasmonics-based devices to avoid the diffraction limit commonly found in the sub wavelength devices has attracted the attention of researchers now a days. As a result of the demand of plasmonics-based devices the necessity of a plasmonic coupler has also increased to make these plasmonic-based devices compatible with the existing non-plasmonic devices. In this thesis, efficient coupling of light between the dielectric waveguide and plasmonic waveguide of metal-dielectric-metal (MDM) type has been investigated theoretically in three dimensions. A novel nano-plasmonic semi-elliptical structure of silicon (Si) has been used as a coupler that connects these waveguides. Finite Integration Technique (FIT) has been deployed for the investigation. A theoretical coupling efficiency of $\sim$78% at optical communication wavelength (1550 nm) has been achieved through numerical simulations. Later on, an air gap was inserted between the dielectric waveguide and the plasmonic waveguide which has improved the efficiency to $\sim$85% near 1550 nm. The dependency of coupling efficiency has been investigated by varying the curvature of the semi-elliptical coupler, the air gap width between the two waveguides, and the width of the air gap of MDM (Ag-Air-Ag) waveguide, and an optimal dimension of the proposed structure has been determined. A number of performance parameters like coupling efficiency, reflection coefficient, return loss, and voltage standing wave ratio (VSWR) have been analyzed with the obtained optimal dimensions for both of the cases. A broad range of operating frequency, tolerance to angular and air gap misalignment and excellent agreement to a demonstrated experimental coupler has made the proposed coupler distinctive.

Chapter 1

Introduction and Background

Surface plasmon polariton (SPP) has got much attention from a different scientific community like materials scientists, physicists even biologists. SPPs have got many potential and new applications due to their distinctive characteristics. SPPs have enhanced localization i.e. local electric fields. Also in the case of SPP, the realization of photons manipulation in the near-field region is possible avoiding the diffraction limit. A significant portion of nanophotonics has been constituted with SPPs nowadays. By controlling and manipulating photons with the help of SPPs in the nano-scale devices with very minute elements, it's possible to exhibit a lot of benefits and challenges like enhanced performance, better efficiency, and significant stability. Optimal use and design of different materials may help to realize different optically integrated SPP nanotechnology-based devices. To be specific, SPP opens up novel and potential ways to different fields involving the environmental, biological, chemical, medical, and health sciences.

1.1 Physics of Surface Plasmon Polariton

1.1.1 SPP Exitation and Coupling

SPPs are surface electromagnetic waves that propagate along with the interface between a metal and a dielectric material, and the surface electromagnetic waves are comprised of surface charges. At the very beginning, it's important to excite these types of charges. To excite these charges, let's consider a p-polarized wave with TM mode i.e. the vector of the electric field is parallel to the incident plane. If this wave reaches an interface that is plane as well as smooth at an incident angle of θ_1 (Figure 1.1a) then the incident wave will have a photon momentum of $\hbar k_d$ (where $k_d = 2\pi n_d$) in the dielectric medium having a refractive index of n_d [1]. When this wave reaches the junction of the two mediums, the reflective wave transmits along a direction with an angle equal to the angle of incidence conserving the photon momentum. On

1
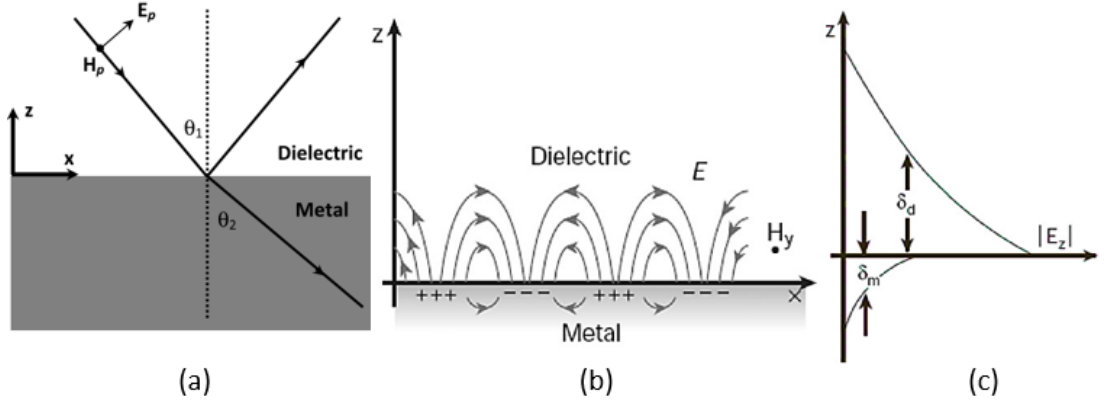
Figure 1.1: (a) p-polarized EM radiation representation, (b) Schematic representation of EM wave and surface charges at the interface of the dielectric and metal, (c) local electric field component is high close to the surface and decay rapidly with distance in a direction normal to the interface. material

the other hand, the wave inside the metal gets propagated in another direction having a refractive angle of θ_2. The momentum of the photon in this case is $\hbar k_m$ (where k_m = $2\pi n_m$) in the metal with a refractive index of n_m, and the component of momentum along the x-direction has been conserved [1]. Now according to Snell's law,

$$n_d\sin\theta_1 = n_m\sin\theta_2 \tag{1.1}$$

Normally, the refractive index of the metal, n_m is less than the refractive index of the dielectric, n_d at the visible wavelength regions, such as for Cu, $n_m = 0.826$ at 563.5 nm, $n_m = 0.272$ at 619.9 nm; for Au, $n_m = 0.608$ at 516.6 nm, $n_m = 0.306$ at 563.6 nm; for Ag, $n_m = 0.173$ at 400 nm, $n_m = 0.120$ at 563.6 nm [12]. Since, $n_m < n_d$ for these wavelength regions, the highest value of refractive angle, θ_2 is 90°, and the incident angle θ_1 is limited to a certain value. Above this limiting angle, the wave will not be able to propagate in the metal. This limiting angle of incidence is known as the critical angle (θ_c), which can be obtained by

$$\sin\theta_c = n_m/n_d \tag{1.2}$$

When there is an incident of p-polarized wave on the interface, the electric field which is in oscillation will cause surface charges at the interface of dielectric and metal to undergo oscillation collectively. Even though the wave got reflected totally at the interface, there remain oscillating charges which have associated fields of radiation that penetrate the metal. These are evanescent or decaying fields along with the direction normal to the junction or interface of the two mediums Figure 1.1 b, c. The decay length is infinite at the critical angle but it decreases very fast to the order of the wavelength of light as the incident angle is increased further. Here, for coupling radiation to

SPPs, the evanescent or decaying fields for the incident wave above the critical angle are helpful. Considering the *x*-axis as direction of propagation and *z*-axis normal to the interface, wave vector of SPP (k_{spp}) is expressed deploying the dispersion relation as [13],

$$k_{spp} = k_0 \sqrt{\frac{\varepsilon_d \varepsilon_m}{(\varepsilon_d + \varepsilon_m)}}. \tag{1.3}$$

Where,

$k_0 = \frac{\omega}{c}$ represents the wave vector in the free space.

Due to the strong light-matter interaction, the SPPs has opened up many possibilities in the field of nanotechnology.

1.1.2 SPP Propagation
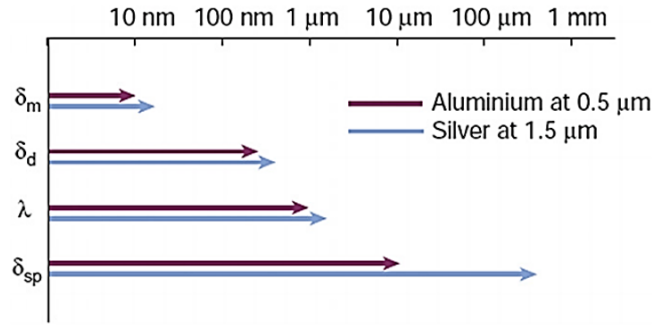
Figure 1.2: Lengths of propagation of SPPs in two different metals [1].

When light is transferred to SPP mode on a flat and smooth metal surface, it will propagate along with the interface of two materials. But, due to the losses arising from the high absorption in the metal the wave will attenuate very fast. Thus, the length of propagation of SPPs is limited by the imaginary part of the complex SPP wave vector (k_x) due to the damping inside i.e. ohmic losses. Where,

$$k_{spp} = k_{sppr} + k_{sppi} \tag{1.4}$$

$$\delta_{spp} = \frac{1}{2k_{sppi}} = \frac{\lambda}{2\pi} \left(\frac{\varepsilon_d + \varepsilon_{mr}}{\varepsilon_d \varepsilon_{mr}}\right)^{3/2} \frac{\varepsilon_{mr}^2}{\varepsilon_{mi}} \tag{1.5}$$

Where, k_{sppr}, k_{sppi} represent the real and imaginary part of the SPP wave vector in the free space respectively and ε_{mr}, ε_{mr} represent the real and imaginary part of the dielectric function of the metal respectively. The length of propagation of SPPs is influenced by the metal's dielectric constant and the wavelength of the incident wave. It can be realized from Equation (1.5) [13, 14]. For instance, aluminum is a comparatively

absorbing metal for which the length of propagation is 2 μm at a wavelength of 500 nm. In the contrary, for a metal of low loss like silver the propagation length is 20 μm at the same wavelength. It has been depicted in fig. Besides, for larger wavelengths like telecommunication wavelength i.e. 1550 nm, the length of propagation of silver rises to even 1 mm.

1.2 Applications of SPP

The ability to control light at a scale much smaller than that of the wavelength of light by exciting SPPs and different unique properties of SPPs have opened doors of diverse applications for SPP-based devices. SPPs have got many potential applications by this time. For instance, chemical and biosensors [15–18], Surface-enhanced Raman spectroscopy (SERS) [19–21], storing data [22,23], solar cells [24,25], subwavelength sources [26,27], subwavelength waveguides [28,29], and so on.

1.3 Metal-Dielectric-Metal Plasmonic Waveguides
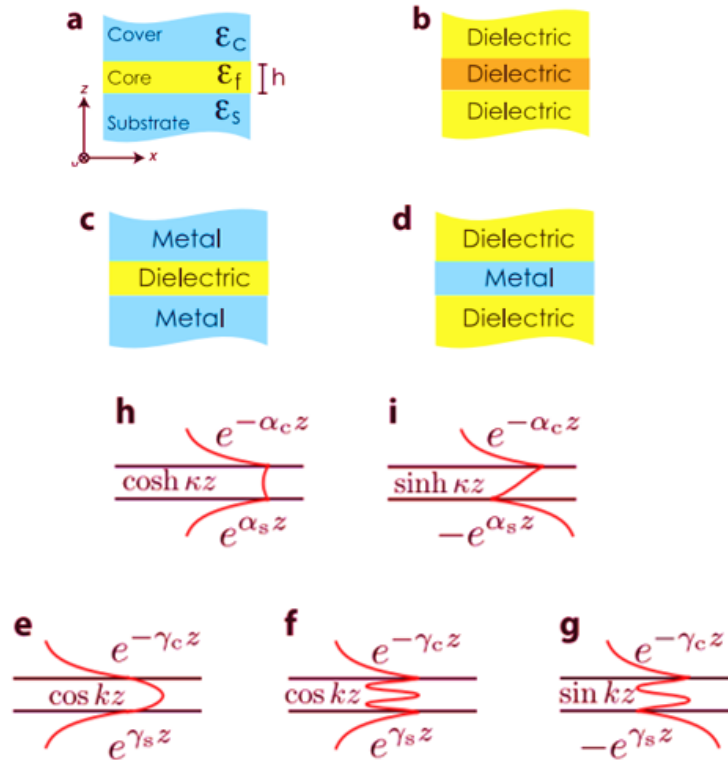
Figure 1.3: Three-layer infinite slab waveguide geometries (a to d) and modes. Typical magnetic field profiles are plotted from e to i. [2].

Two different materials with opposite dielectric constant (positive and negative) are needed for the generation of surface plasmon polaritons (SPPs). At the interface of

these two materials, SPPs will be generated and propagated. As the dielectric constant of the metal is negative, different nanostructures and devices have already been proposed by this time using metals deploying the characteristics of SPPs. These nanodevices include metallic thin film, nanorods, nanohole, nano grooves, chained particles, metal-dielectric-metal (MDM) waveguide, dielectric-metal-dielectric (DMD) waveguide, and so on [2]. Figure 1.3 shows a few possible waveguide geometries among which Figure 1.3 c,d can be used as a plasmonic waveguide. Figure 1.3 e-i depicts different possible modes of the waveguide. Actually, the localization of the electromagnetic field and its propagation loss are the two parameters that should be considered for the above-mentioned types of devices. The DMD-based nanostructure can travel a comparatively large distance. By the way, they provide poor localization of electric field. On the other hand, MDM waveguide has more propagation loss thus the propagation length is less. But, they are capable of confining light into the subwavelength scales. Thus it opens up the way to interconnect the highly integrated electronic circuit along with the optical circuit on the same chip where both photons and electrons are important in carrying the information.

1.4   Plasmonic Couplers

The MDM structure mentioned in the previous section comes with exponentially increasing losses, limiting the propagation to the order of nanometers. This disadvantage can be overcome through the use of dielectric waveguides, which can transmit signals over large distances. Thus, both of the waveguides are important. This kind of hybrid setup calls for the efficient coupling of the two types of waveguides. The use of a coupler will enhance the transfer of signal from dielectric to the plasmonic waveguide and vice versa. Figure 1.5 demonstrates how the coupler will help to enhance

Table 1.1: Performance of different plasmonic couplers

Ref.	Structural design	Efficiency %	Year
[30]	Lateral taper funnel coupler	33%	2010
[31]	Air-Slot coupler Toward Dense Optical ICs	40%	2015
[32]	Slot-to-slot plasmonic coupler	43%	2010
[33]	Slot-to-slot coupling	50%	2016
[5]	Si based rectangular coupler	70%	2007
[3]	Hybrid linear tapered plasmonic coupler	60-70%	2010
[34]	Wideband plasmonic slot-silicon waveguide couplers	70%	2010
[35]	Nanoplasmonic Air-Slot Coupler	50%	2012

[36]	Symmetrically corrugated si based plasmonic coupler	73%	2012
[37]	Hybrid metal–insulator plasmonic directional coupler	75%	2013
[4]	Cuprous oxide-based rectangular coupler	56%	2014
[11]	AlAs based rectangular coupler	60%	2015
[11]	Alumina based rectangular coupler	50%	2015
[10]	GLS based rectangular coupler	67%	2014
[38]	Integrated nanoplasmonic air-gap coupler	70%	2014
[39]	Slot-to-slot coupling	73%	2014
[40]	Nano-coupler between MIM and dielectric slab waveguides	75%	2018
[8]	Air Slot nano-plasmonic coupler	81%	2020
[41]	Lens funnel coupler	81%	2019

the transmittance of the signal from one to the other for a silver-GLS-silver plasmonic waveguide with the same dimensions. Without a coupler, the transmission efficiency is around 59.17% [42], whereas, with a coupler, it enhances to around 71% [43]. This is how the plasmonic couplers became a research field of interest for many researchers.
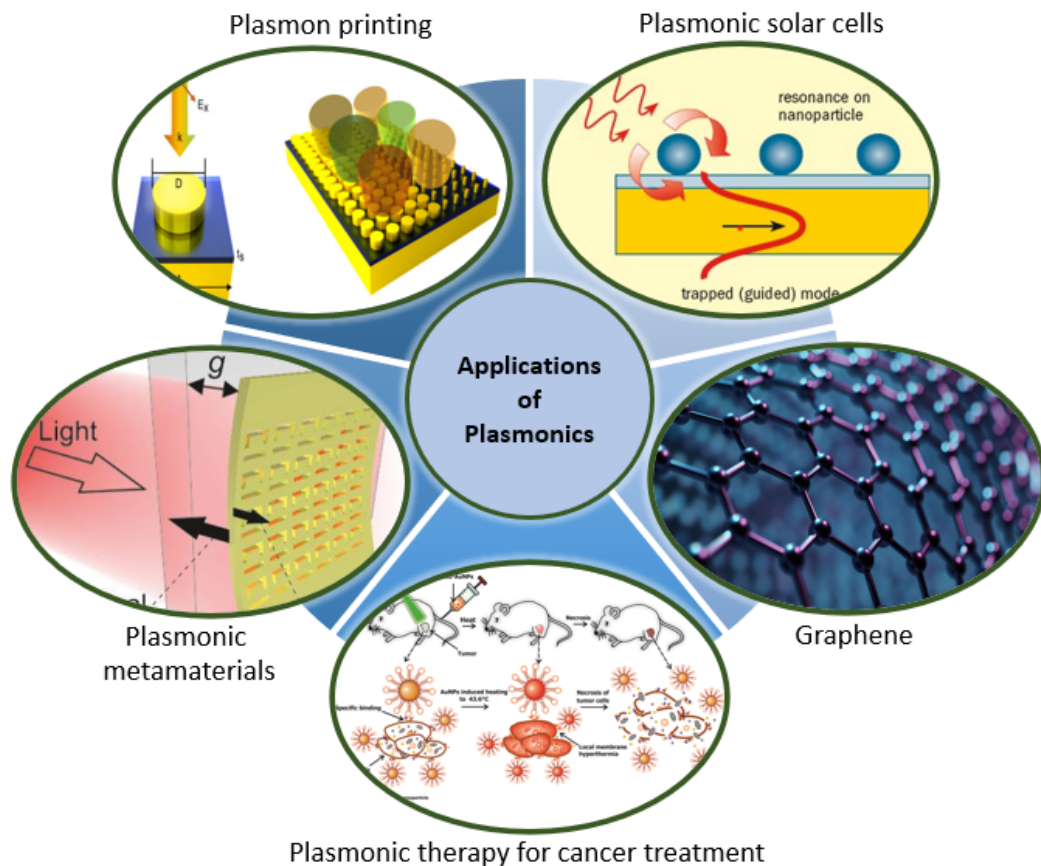
Figure 1.4: Diverse applications of plasmonics.

1.5 Literature Review

Plasmonics, capable of unifying electronics and photonics [44], is one of the promising subdisciplines of nanophotonics, which has attracted much attention in recent years due to its incredible ability to overcome diffraction limit. This limit provides a critical regions as little as just a few nanometers [2]. Plasmonics with its unprecedented ability of light confinement and substantial light-matter interactions has already opened up many opportunities like subwavelength imaging and superlenses [45–48], chemical and biological sensing [49–52], plasmonic solar cells [53–56], plasmonic metamaterials [57–60], and properties of surface plasmon arising from surface electron accumulation (SEA) [61], optical devices [62–64], plasmon printing [65–67], quantum dot plasmonics [68–70], plasmonic therapy for cancer treatment [71–74], graphene [75–77], invisible cloak [78–80],and so on. These interdisciplinary applications prospect how far plasmonics can go. Figure 1.4 depicts a few applications of plasmonics which indicates how diversified the implimentation of plasmonics is.

The waveguides can be implemented in the optical devices in the nanometer range [81]. Nowadays, plasmonic waveguides have been anticipated to be an eligible candidate for the upcoming highly integrated photonic circuits. Several distinct plasmonic
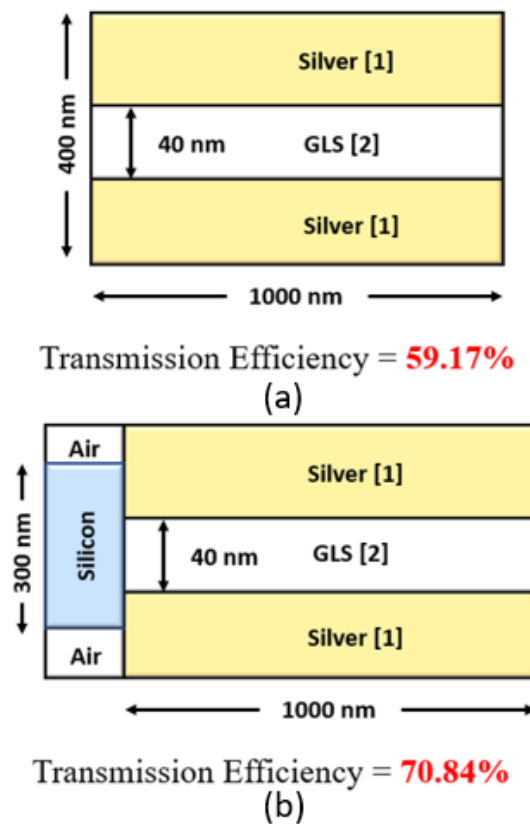
Figure 1.5: Representation of the effect of plasmonic couplers (a) without coupler, (b) with a coupler.

waveguides have been proposed and analyzed so far, such as metal nanoparticle plasmon waveguides [82–84], integrated metal slot waveguide [85], hybrid plasmonic waveguides [86–89], metallic nanowires [90, 91], stripe waveguides [92] and so on. Particularly, metal-dielectric-metal (MDM) plasmonic waveguide has the incredible ability to guide optical signals in subwavelength scale through surface plasmon polaritons (SPPs). Research work on MDM configuration of SPP waveguides has made major advances in superlens [93], hyperlens [94], channel plasmon-polariton (CPP) [95], splitters [6], Bragg reflectors [96], and many more.

Above all, there is a trade-off between the mode confinement and propagation length of these MDM plasmonic waveguides. This limitation of propagation length is due to the propagation loss of SPP in one of the major constituent material, metal. To overcome this problem, it is imperative to use both dielectric waveguide and MDM waveguide in the same platform. Propagation loss will be compensated by the dielectric waveguide and for dealing with subwavelength scale optoelectronic devices, MDM waveguides will be utilized. Thus, it is indispensable to place a coupler between the two waveguides following the essence of efficient coupling between them. Several techniques for efficient coupling have been proposed like nanoplasmonic coupler with multi-section tapers [5], nanoplasmonic air-slot coupler [35], $\lambda/4$ coupler [7], semi-elliptical coupler [97], adiabatic and non-adiabatic tapered plasmonic coupler [98], and others. Performance of different types of couplers proposed so far by different authors has been summarized in Table 1.1. Optimization of shape, size, and topology of plasmonic nanostructures like couplers, antennas, and others were reported in [99–101] to get the most out of the novel structures.
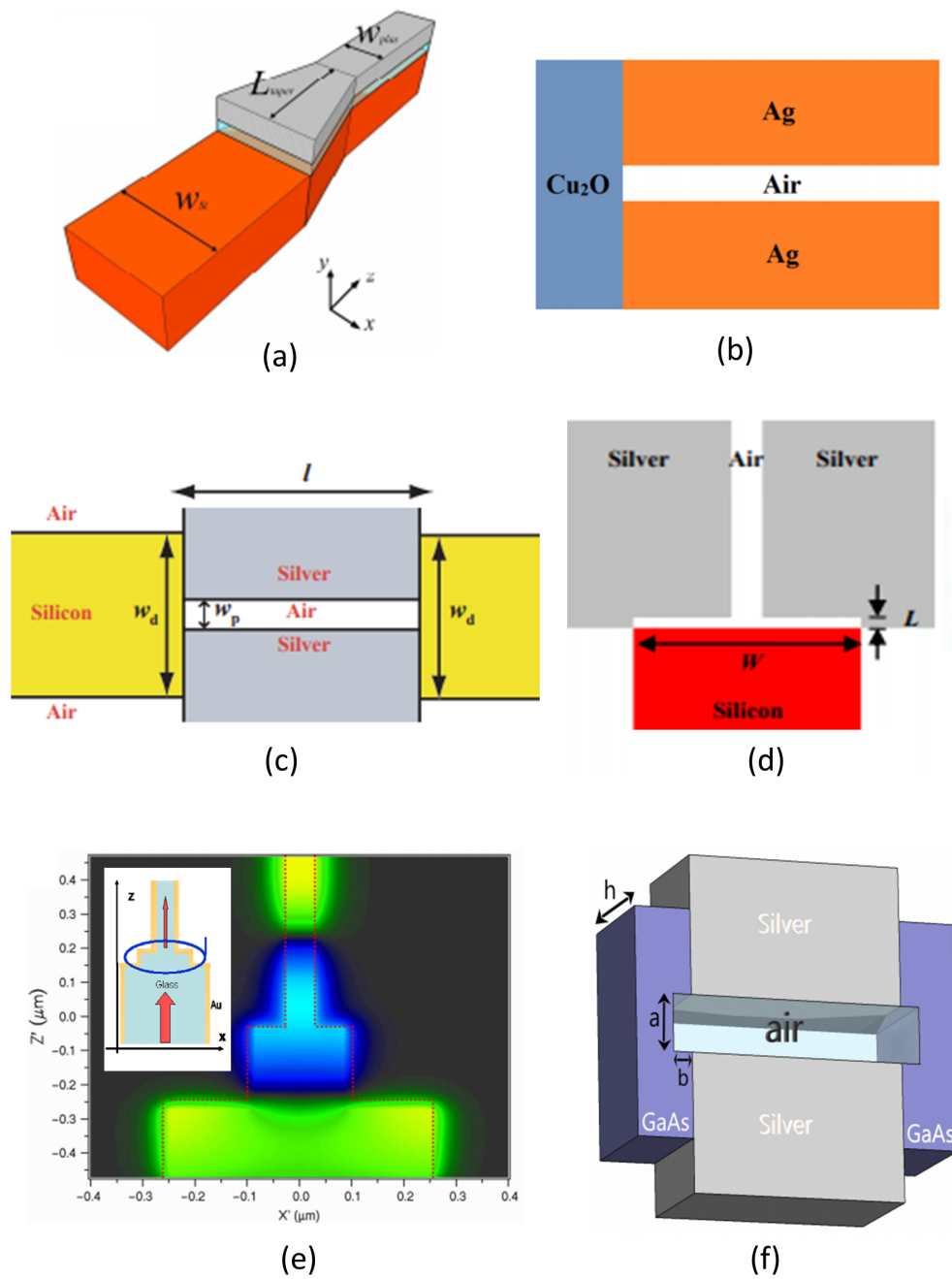
Figure 1.6: Different types of already demonstrated plasmonic couplers
(a) Hybrid linear tapered plasmonic coupler [3],
(b) cuprous oxide-based ultra-compact nanoplasmonic coupler [4],
(c) rectangular compact plasmonic coupler [5],
(d) air gap based rectangular plasmonic coupler [6],
(e) $\lambda/4$ coupler with field profile [7],
(f) air slot nano-plasmonic coupler [8].

1.6 Thesis Objective

The objectives of this thesis with specific aims are:

- To propose a simple semi-elliptical nanoplasmonic coupler that provides better transmission efficiency and which is easier to fabricate.

- To optimize the proposed structure prioritizing the transmittance of the plasmonic coupler.

- To investigate different performance parameters of the final coupling structure after optimization.

- To do the above three steps for air gap based semi-elliptical nanoplasmonic coupler.

1.7 Thesis Organization

The thesis has been arranged in the following way:

- Chapter 1 presents a brief introduction to surface plasmon polaritons along with their applications. The recent development in plasmonic metal-dielectric-metal waveguides has been discussed. This chapter also includes a brief description of plasmonic couplers. Chapter 1 concludes with the thesis objective and thesis outline.

- Chapter 2 gives idea on electromagnetic waves. This includes Maxwell's four equations and generalized constitutive relations to realize Maxwell's equation for different media.

- Chapter 3 presents the methodology of the research. It describes the finite integration technique (FIT) and the method of simulations. It includes the verification of the methodology used based on an already published article.

- Chapter 4 proposes a novel semi-elliptical nanoplasmonic coupler. It includes the discussion on results obtained based on different performance parameters. It also depicts the advantages of the proposed coupler compared to the previous couplers.

- Chapter 5 details a novel air gap-based semi-elliptical nanoplasmonic coupler. It includes the discussion on results obtained based on different performance parameters. It also depicts the advantages of the proposed air gap-based semi-elliptical nanoplasmonic coupler compared to the previous couplers.

- Chapter 6 concludes by summarizing the whole work. Where a brief idea of the proposed simple and air gap-based semi-elliptical nanoplasmonic coupler has been given. Along with this it gives the future works based on the present work. An idea of a new coupling structure named graded air gap-based semi-elliptical nanoplasmonic coupler has been given along with the possible potentials of the couplers. Way to fabricate the proposed structure has also been suggested in this chapter.

Chapter 2

Electromagnetic Waves

The electromagnetic wave is always present and all around us. Natural or man-made electromagnetic energy can come from either earthly or interplanetary sources. Energy encoded with information is emitted by electrical equipment and is the source of an attacker's emanations. These emanations are electromagnetic waves, and they follow the fundamental physical laws described in this chapter. As a result, these rules regulate the behavior of signals that need to be protected from tampering. The argument is that knowing these concepts can aid in the development of successful information security solutions.

Since 1864, when British scientist James Clerk Maxwell (1831–1879) first established the fundamental equations of electromagnetism, many texts and articles have been produced on the subject. Heinrich Hertz (1857–94), a German scientist, followed Maxwell's equations with experiments that demonstrated the presence of electromagnetic waves. The intricacies of electromagnetic energy's interaction with materials are now well known, and they are also critical to a greater understanding of the sensitivity to signal identification and, eventually, data compromise.

2.1 Electromagnetic Fields and Flux

2.1.1 Electromagnetic Fields

Electromagnetic waves are transverse waves. Alternatively, the propagation direction is orthogonal to the mutually perpendicular oscillation planes of the magnetic and electric fields. These fields are the constituents of an electromagnetic energy wave. Figure 2.1 depicts an electromagnetic wave in motion.

The forces exerted by electric and magnetic fields on static and moving test charges, respectively, are used to characterize these fields. Because electric and magnetic fields are vector quantities, they each have a magnitude and a direction. There are several examples of vector forces, and lines related to the force they exert can provide a simple
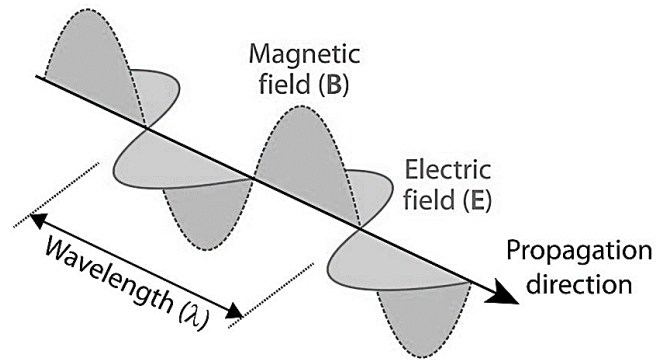
Figure 2.1: An electromagnetic wave

method to visually represent them. A greater density of lines implies a greater force. Such forces have an impact on data transfer, absorption, and reflection, as well as data security.

Because electric fields apply forces on charged particles, vectors are useful for characterizing the field's direction and amplitude. Except when traveling perpendicular to the field, magnetic fields do not directly impose forces on charged particles. Varying magnetic fields, on the other hand, produce electric fields, which in turn impose similar forces. It is one of the major outcomes of Maxwell's equations, which will be explored more in this chapter. Magnetic fields originate exclusively from moving charges, such as currents, whereas electric fields are connected with both static and moving charges.

2.1.2 Electric and Magnetic Flux

As stated previously, the strength of a magnetic or electric field is related to the density of its associated lines of force in a region of space. These lines of force are connected to the magnetic or electric flux, a physical quantity that is fundamental to electromagnetic processes as defined by Maxwell's equations. Since it is the rate of change of electric and magnetic flux with the time that results in the magnetic and electric fields generation, a definition of flux is given straight immediately.

The electric flux (Ψ) across a surface with an area of A which is orthogonal to the direction of the electric field E is described as follows:

$$\Psi = \varepsilon E A \tag{2.1}$$

where ε = dielectric constant or relative electric permittivity. In other words, electric flux is the total number of electric field lines passing through a surface of area, A.

In identical analogy, the magnetic flux Φ) across a surface with an area of A that is orthogonal to the magnetic field B is defined as follows:

$$\Phi = B\mu A \tag{2.2}$$

where μ = the permittivity of free space. In other words, magnetic flux is the total number of magnetic field lines passing through a surface of area, A.

The idea of flux is vital in comprehending electromagnetic phenomena and, as a result, to comprehending the fundamentals of information security. It could be advantageous to use an analogy with a more intuitive physical quantity.

Imagine a rectangular loop or surface with an area of A. With a velocity of v, water flows over the plane of this loop. Let's pretend the water is running perpendicular to the plane of A for the sake of simplicity, but keep in mind that this is a particular situation because the water might be flowing at an angle to the loop. The volume of water per unit time v that travels across the cross-sectional area A is the flux of water over the imaginary surface in this geometry. As a result, the water flux

$$\Phi_w = vA \tag{2.3}$$

2.2 Maxwell's Equations

All electromagnetic phenomena can be described by Maxwell's four equations. It seems remarkable that four compact expressions describe all electromagnetic phenomena but it is true.
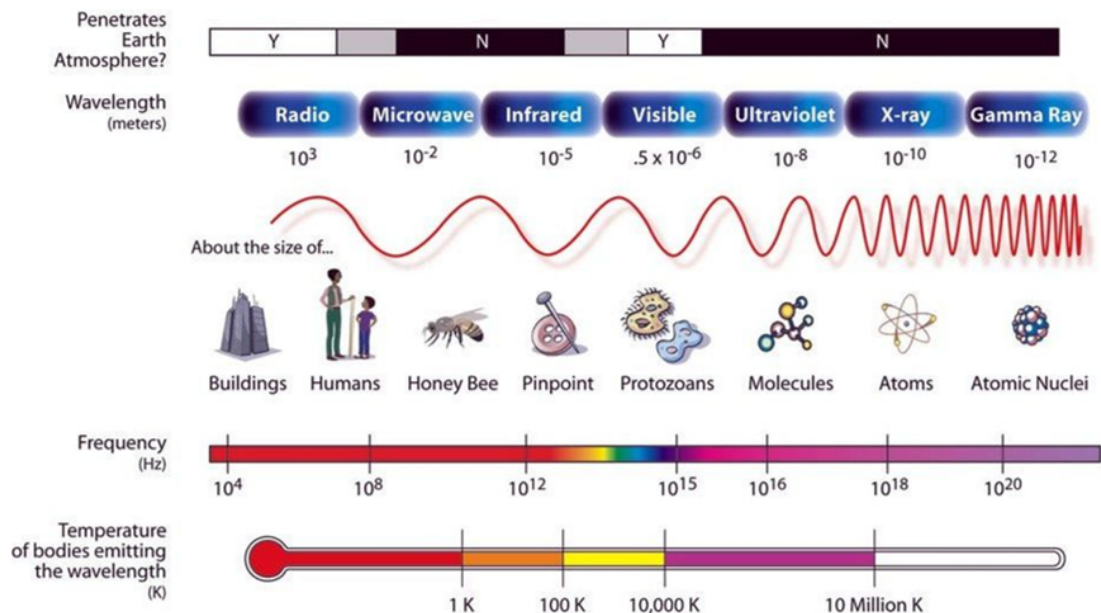
Figure 2.2: The electromagnetic spectrum

Figure 2.2 depicts the electromagnetic radiation spectrum, which, as the phrase

goes, extends from "DC to Daylight". It also depicts the connection between temperature and wavelength, which is crucial in the analysis of thermal noise. The equations of Maxwell can be expressed in differential or integral form, but the idea is the same.

The first equation is termed Gauss's Law. The electric flux over a surface is proportional to the charge contained by that surface q_{enc}, as per this equation. In a nutshell, the second equation states that there are no isolated sources of magnetic fields. According to the third equation, the rate of change in magnetic flux over time results in changing electric fields. Lastly, the fourth equation states that electric currents cause magnetic fields to form. The simplistic form of these statements belies their importance.

The interrelationship between electric and magnetic fields is described by Maxwell's law, which is made up of four basic electromagnetic phenomena (Faradays' law, Maxwell-Amperes' law, Gauss's law of the electric and magnetic form). The integral and differential versions of the equations are well-known and widely utilized in the study of electromagnetic problems. The differential version of Maxwell's equations is provided in this section. Maxwell's equation may be written as follows for a time-varying electric and magnetic field:

$$\Delta \times E = -\frac{\partial B}{\partial t}, \qquad [Faraday'sLaw] \qquad (2.4)$$

$$\Delta \times H = J + \frac{\partial D}{\partial x}, \qquad [Ampere - Maxwell'sLaw] \qquad (2.5)$$

$$\Delta . D = \rho, \qquad [Gauss'sLaw] \qquad (2.6)$$

$$\Delta . B = 0. \qquad [Gauss'sLawformagnetism] \qquad (2.7)$$

Here,

E = electric field intensity

H = magnetic field intensity,

D = electric flux densities,

B = magnetic flux densities,

J = electric current density, and

ρ = volume charge density.

The continuity equation, often known as the law of conservation of charge, is a mathematical formula that connects the electric current density and the volume charge density. It is written as,

$$\Delta.J = -\frac{\partial P}{\partial t}. \tag{2.8}$$

The differential form necessitates an understanding of the curl and divergence (div) operators that appear to be less intuitive than the integral form. Besides, for FIT the integral form of Maxwell's equations is needed. In the following, the integral form of Maxwell's four equation has been given:

$$\oint E.dA = \frac{q_{enc}}{\varepsilon_0} \tag{2.9}$$

$$\oint B.dA = 0 \tag{2.10}$$

$$\oint E.ds = -\frac{d\phi_s}{dt} \tag{2.11}$$

$$\oint B.ds = \mu_0\varepsilon_0\frac{d\phi_E}{dt} + \varepsilon_0 i_{enc} \tag{2.12}$$

These four equations may look difficult at first, but they can be understood using the terminology and ideas listed below. Their inclusion in an information security discussion stems from the fact that they describe the behavior of all electromagnetic phenomena, including the fields associated with communications intercepted by hackers.

2.2.1 First Equation

$\Delta\Phi = E\,\Delta A$

$\Phi_{electric} = \frac{Q}{\varepsilon_0}$

The sum of the flux is proportional of the total charge enclosed.
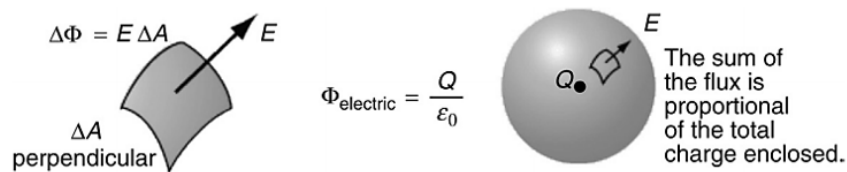
Figure 2.3: Maxwell's first equation, or Gauss's Law.

According to Maxwell's first equation, commonly known as Gauss's Law, the total electric flux across a surface is equal to the total charge Q that exists inside the volume enclosed by that surface. Therefore $\varepsilon EA = Q$.

Gauss's Law implies that there would be no electric field in the absence of electric charges. The flux of E across the surface must be zero if no charges are present within the surface that encloses a volume. The geometry of Gauss's Law has been depicted in Figure 2.3.

Summary of Maxwell's first equation: *The source of electric flux across a surface derives from charges within the volume enclosed by that surface*.

2.2.2 Second Equation
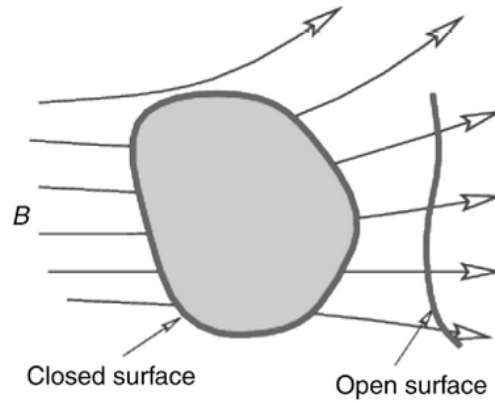
Figure 2.4: Maxwell's second equation and flux across closed and open surfaces.

Maxwell's second equation is identical in form to the very first, but the outcome is significantly different. It is also known as the magnetic equivalent of Gauss's Law due to its symmetry with Gauss's Law.

According to Maxwell's second equation, the surface integral of the magnetic field across a closed surface is zero. To put it in another way, the magnetic field over any surface enclosing a volume is always zero. It can be understood from the identical geometry that exists in Maxwell's first equation. But for the first equation, the flux of the electric field across a surface enclosing a volume is directly related to the charges inside that volume.

The magnetic flux over a closed surface, i.e., a surface that fully encloses a volume with no holes, is seen in Figure 2.4. There is no flux across the surface from the volume contained by that surface, and every field line that approaches the closed surface must depart it in the same way. If the flux lines were not like that, a source of magnetic fields could be there as a stand-alone entity.

Summary of Maxwell's second equation: *Maxwell's second equation can be summarized as follows: There are no magnetic charge sources*.

2.2.3 Third Equation

The production of electric fields from the time rate of change of magnetic flux is described by Maxwell's third equation. This equation explains magnetic induction, in which a change in the magnetic flux produces an electromotive force (EMF) or an electric potential difference. Besides, Maxwell's third equation states that the rate of
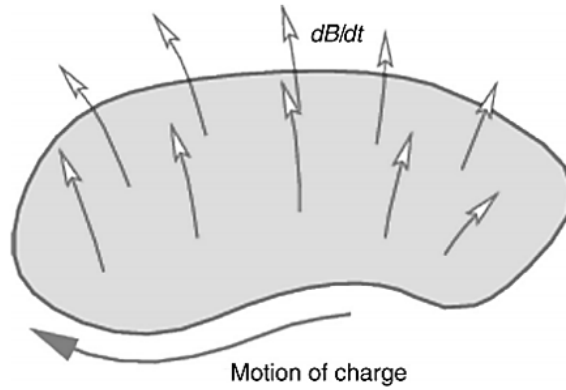
Figure 2.5: Maxwell's third equation, or Faraday's Law

change of the magnetic flux across the surface specified by a boundary creates a changing electric field whose magnitude equals the line integral around that boundary.

For a surface of area A and circumference S, Maxwell's third equation, commonly known as Faraday's Law (named after Michael Faraday, a British physicist),

$$\oint E.ds = \mu A \frac{dH}{dt} = -\frac{d\phi_s}{dt} \tag{2.13}$$

Where,

H = magnetic field

A = surface of area oriented at 90 degrees to H

ϕ = magnetic flux

Total magnetic flux across $A = HA$

The negative sign denotes that if an induced current flows, it will always flow in the opposite direction as the change that caused it. It is a statement of Lenz's Law, which is essentially an expression of energy conservation.

In a nutshell, Faraday's Law explains the creation of electric fields and the accompanying flow of currents owing to the rate of change of magnetic flux with time, as seen in Figure 2.5. Summary of Maxwell's third equation: *Changing electric fields are caused by the rate of change in magnetic flux over time*.

2.2.4 Fourth Equation

The magnetic fields that emerge from currents in the form of time-varying electric flux plus moving charges are described by Maxwell's fourth equation, commonly known as Ampere's Law (named after a French mathematician and physicist, Andre-Marie Ampere).

In part, Maxwell's fourth equation says that the line integral of the magnetic field surrounding a surface is equal to the rate of change of the total electric flux over that
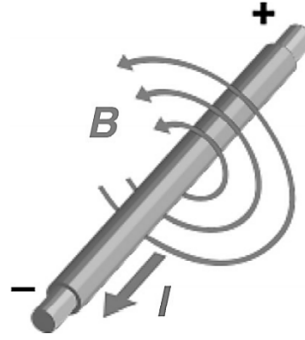
Figure 2.6: Maxwell's fourth equation, alternatively Ampere's Law.

surface. As a result, here is a partial expression for Maxwell's fourth equation:

$$\oint B.ds = \varepsilon A \frac{dE}{dt} = \frac{d\psi}{dt} \tag{2.14}$$

The magnetic field produced due to the presence of a current-carrying wire is seen in Fig. 2.6. Magnetic field magnitude is contributed by moving charges or equivalently the current enclosed by the surface $i_{enclosed}$. Thus the full expression for Maxwell's fourth equation takes into account both moving charges enclosed by the surface and changing electric flux across the surface:

$$\oint B.ds = \frac{d\psi}{dt} + i_{enclosed} \tag{2.15}$$

2.3 Constitutive Relations of Maxwell's Equations

The Maxwell's equation describes the fields created by charge and current without specifying how they are generated. The nature of material in contact with fields is explained by constitutive equations, which allow Maxwell's equations to be applied to a different materials. Constitutive equations can be expressed as,

$$D = \epsilon_0 E + P, \tag{2.16}$$

$$B = \mu_0 (H + M), \tag{2.17}$$

$$J = \sigma E, \tag{2.18}$$

where,

μ_0 = Magnetic permeability of vacuum, (Hm^{-1}),

ϵ_0 = Electric permittivity of vacuum, (Fm^{-1}),

σ = Electric Conductivity, (Sm^{-1}).

Considering the electromagnetic wave propagation in the vacuum , the numerical values of the permeability and permittivity are,

$$\varepsilon_0 = \frac{1}{c_0^2 \mu_0^2} = 8.854 * 10^{-12} Fm^{-1}.$$

$$\mu_0 = 4\pi * 10^{-7} Hm^{-1},$$

Where,**P** denotes the dielectric polarization of the material when there is an influence of the external electric field. It can be considered as the dipole moment in unit volume cell and linearly related to the applied electric field, dielectric constant (ε_0), and the medium's susceptibility (χ_e). Thus,

$$P = \varepsilon_0 \chi_e E. \tag{2.19}$$

In the same way, *M* indicates the magnetization vector under the influence of external magnetic field, *M*. It actually indicates the permanent or temporary magnetic dipole moments in the magnetic materials. *M* also denotes the density of magnetic dipole vector and proportionally related to applied magnetic field, permeability (μ_0) and magnetic susceptibility (χ_m) of the medium. Thus,

$$M = \mu_0 \chi_m H. \tag{2.20}$$

2.3.1 Constitutive Equation for Linear Material

For linear materials, which have constant material properties with the variation of applied field, the constitutive equation can be described as,

$$D = \varepsilon_0 (1 + \chi_e) E = \varepsilon_0 \varepsilon_r E = \varepsilon E, \tag{2.21}$$

$$B = \mu_0 (1 + \chi_m) H = \mu_0 \mu_r H = \mu H, \tag{2.22}$$

where,

$$\varepsilon_r = (1 + \chi_e),$$

$$\mu_r = (1 + \chi_m).$$

2.3.2 Constitutive Equation for Non-Linear Material

For non-linear material, there exists non-zero polarization and magnetization without the presence of external *E*-field and *H*-field. So, an additional term to address the non-zero effect is added with the constitutive equation. Constitutive relation for *E*-field is,

$$D = \varepsilon_0 \varepsilon_r E + D_r. \tag{2.23}$$

Here, D_r denotes the electric flux density with the absence of *E*-field, known as *remanent electric flux density*.

Constitutive relation for *H*-field is,

$$B = \mu_0 \mu_r H + B_r. \tag{2.24}$$

Here, B_r denotes the magnetic flux density with the absence of *H*-field known as *remanent magnetic flux density*.

Chapter 3

Methodology

3.1 Finite Integration Techniques (FIT)

3.1.1 Definition and Application of FIT

The Finite Integration Technique (FIT) is a consistent discretization scheme for Maxwell's equations in their integral form. Discretized fields matrix equations which are obtained as a result of FIT helps to give efficient numerical simulations. Besides, this helps to prove the conservation properties of charge and energy. On the other hand, in time domain it gives numerical formulations stability property. Thus, FIT can be told as the method of numerical simulation for Maxwell's equation without any approximation in the integration form.

Its application can be found in different software like CST (Computer Simulation Technology) MICROWAVE STUDIO and MAFIA where FIT is the mathematical base.

3.1.2 Basics of FIT

Historically, before three decades, Weiland et al. (1977) first demonstrated the finite integration technique (FIT) in electrodynamics, where FIT was applied to the full set of Maxwell's equations in integral form [102]. This method deploys all six vector components of magnetic flux density and electric field strength on a dual grid system. FIT gives Maxwell's equations discrete reformulation in their integral forms which are perfect for computers. Besides, this allows simulating real-world electromagnetic field problems having complex geometries.

This mathematical background of FIT is connected to the conformal Edge-Finite-Element schemes which are employed in computational electromagnetics. These are, in general, derived starting from mathematical variational formulations.

3.1.3 Advantages and disadvantages

Many of the benefits of FIT are similar to those of the FDTD technique, such as ease of implementation and effective parallel computation. It also mitigates some of the FDTD's drawbacks. On the full domain and in each discretization cell, this finite volume type discretization for Maxwell's equations fulfills equations like Faraday's law. In this respect, FIT enables the proof of discrete field conservation characteristics in an inhomogeneous medium [103]. The use of the Yee [104] Cartesian mesh, which is inflexible when complicated and nonorthogonal structures are discretized, is the most prevalent drawback of the finite integration approach, similar to the FDTD method.

The explicit formulation of the FIT, like the FDTD, has the significant disadvantage of the time step being dependent on the grid size depending on the CFL condition. Particularly for applications requiring very tiny mesh sizes, such as lithography simulation. The time step becomes considerably smaller in this scenario, resulting in a longer simulation period.

In a updated study of FIT [105], the concept and several implementations of this method for a variety of applications are presented. A wide range of scattering problems [106, 107], magnetic equipment [108], radio frequency and microwave modeling [109], dielectric resonators [110], electromagnetic field in internal organs [111], dispersive media [112], and solar cells [113] are among the most potential applications in electromagnetic problems.

3.2 Outline of Methodology

After completing the literature review, one specific coupler which has been demonstrated theoretically as well as experimentally [9] has been chosen as a benchmark problem. That coupler has been resimulated in the CST. It was checked if its performance related to transmittance is matching with the experimental one of the benchmarked problem or not. If it does not match then again the structure was modeled in the CST and this would continue till the transmittance curve of the simulated one matches with the experimental one. Once the results match, the validity of the simulation was clear. Thus based on that simulation conditions, the structure was modified and different performance parameters were measured. It would go for the repeated structural modification until an improved result is found. When the improved results were available, then optimization was done to get the final proposed structure. The overall outline of methodology that has been followed to get the best possible outcome from the simulation has been depicted in Section 3.2.
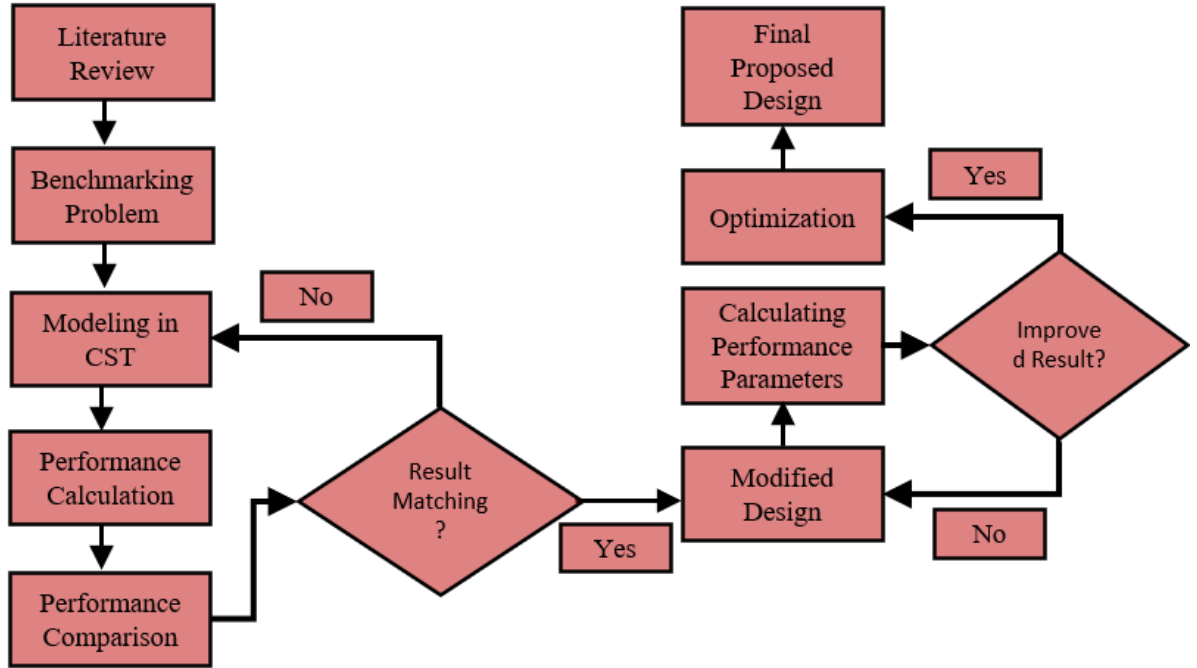
Figure 3.1: Overall outline of methodology

3.3 Simulation Steps

For investigating the properties of the proposed coupler, finite integration technique (FIT) has been implemented. FIT is a spatially discretized scheme for solving electromagnetic field problems numerically in both frequency and time domains. Vital topological properties of different continuous equations like conservation of energy and charge are preserved in FIT, which is important for our case. FIT is the basis for different simulation tools as it covers almost a full range of optical applications and electromagnetics. Three-dimensional electromagnetic (EM) simulation software, CST MICROWAVE STUDIO (CST MWS), is used as the simulation tool. A time-domain solver has been used in our simulation. The simulation settings used in the analysis include hexahedral mesh property, 15 cells per wavelength, 20 cells per maximum model box edge, and a total of 109,200 mesh cells. CST MWS in the time domain provides the scope of using experimental data directly in the case of the frequency-dependent dielectric constant of metals (such as silver and gold) [12]. The steps for simulations of plasmonic nanostructures has been depicted in figure Section 3.3.

All the boundaries of the proposed structure in the simulation domain are kept open to get the advantages of the perfectly matched layer (PML) [114] as well as to prevent back reflections after attenuating fields within the boundary regions. Fundamental mode has been excited at the input terminal to investigate different performance pa-

Simulation Steps
CST Studio Suite ®

#	Step
1	Open CST MWS
2	Create new template
3	Choose application area / MW, RT & optical
4	Choose application area / Optical application
5	Choose workflow / Plasmonic/metallic structure
6	Choose workflow / Plasmonic waveguide
7	Choose solver / Time domain
8	Choose units / Dimensions, frequency, time, temperature, etc.
9	Modify settings / Wavelength range, monitors, etc.
10	Summarize template / Name the template
11	Define materials
12	Define/model structure
13	Define mesh
14	Customize view
15	Define waveguide ports / Port 1 and port 2
16	Define boundary conditions
17	Setup solver / Select time domain solver
18	Specify time domain parameters
19	Start simulation
20	Post processing
21	Result analysis

Figure 3.2: Simulation steps exclusively for the CST MWS

rameters like coupling efficiency, transmission and reflection coefficients, absorbance, VSWR, and return loss. Coupling efficiency is calculated by the ratio of the power

obtained from ports placed at the input and output sides of the Si waveguide. The received power is measured just after the interface of the MDM and plasmonic waveguide. As a precaution to avoid the contributions of radiative modes in the measurement of power, a small distance of 5 nm has been considered while placing the port beside the interface.

3.4 Experimental Validation

To validate our simulation, the air-slot coupler demonstrated by Rami A. Wahsheh *et al.* [9] has been re-simulated. The two-dimensional finite-difference-time-domain (FDTD) method has been used in their design and analysis. Due to the long run time and large memory requirements for 3D simulations, Rami A. Wahsheh *et al.* [9] performed 2D FDTD simulation and compared their result with the results obtained through the analysis of a 3D experimental structure. Using FIT, we have successfully simulated the 3D experimental structure of Rami A. Wahsheh, which shows excellent agreement with experimental data, particularly within the wavelength range of 1500 to 1620 nm. The dielectric material and metal that they have used are silicon and gold respectively.
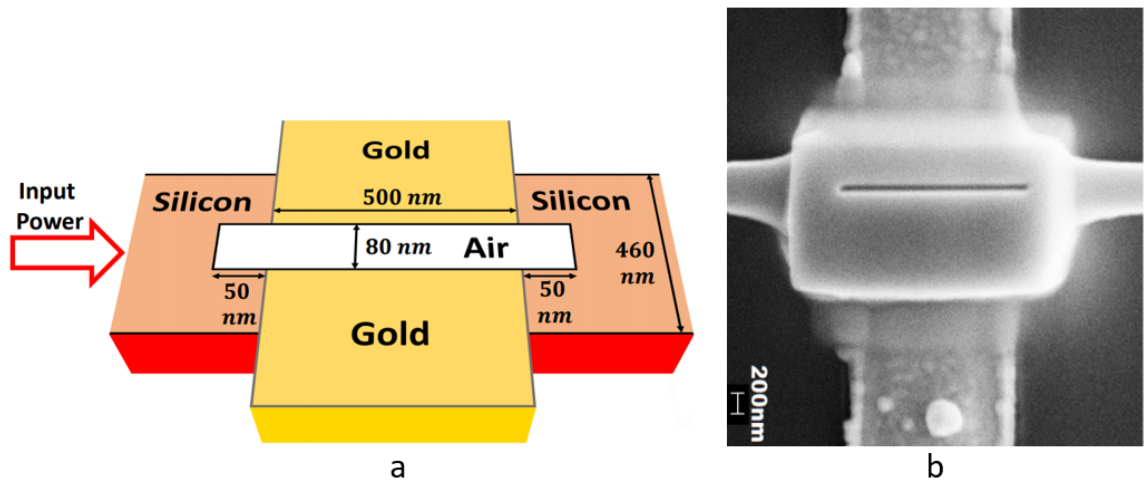
Figure 3.3: Plasmonic air-slot coupler demonstrated by Wahsheh at el. [9] (a) Three dimensional schematic, (b) Scanning electron microscope image of the fabricated air-slot coupler

The geometry of the experimental structure that has been simulated is shown in Section 3.4.

The coupling efficiency has been analyzed by normalizing the output power with respect to the input power. Variation of normalized power with wavelength has been demonstrated in Section 3.4. Experimental spectrum of the fabricated plasmonic coupler is analogous to that of the simulation of Rami A. Wahsheh *et al.* [9] when shifted to
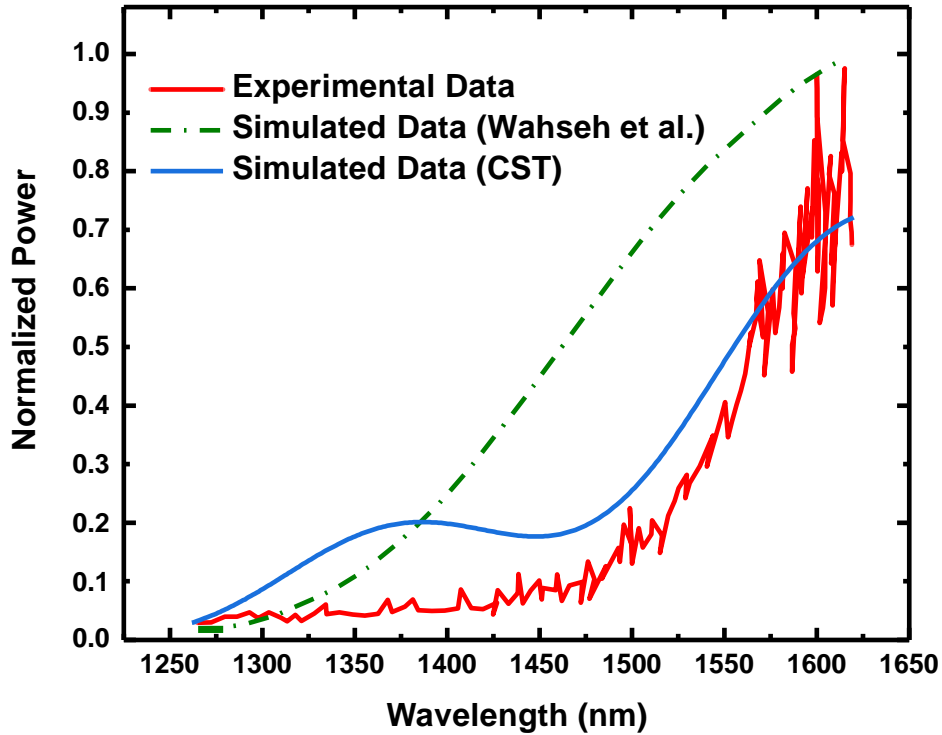
Figure 3.4: Comparison of the experimental [9] and CST simulation results.

110 nm due to lithography and etching bias. Here, we did not consider the 110 nm shift in our simulation. Even without considering the shift we got a curve of the transmission efficiency almost same as the experimental one. Specially, near the telecommunication wavelength of 1500 nm, in ehte range of 1500 nm to 1600 nm they almost coincide each other. The % of error at different wavelengths is tabulated in Table 3.1. From the table, it's clear that, the average deviation of the efficiency is around 6% within the range of 1500 nm to 1620 nm, which is far better then the simulation done by Wahsheh *et al.*

Table 3.1: Percentage of error of simulated data and experimental data between wavelengths 1500 nm to 1620 nm.

Wavelength	Experimental Data	Simulated Data	Error (%)
1500	0.224	0.255	13.839
1528	0.288	0.340	18.056
1545	0.381	0.448	17.585
1550	0.406	0.476	17.241
1567	0.545	0.557	2.202
1576	0.598	0.599	0.167
1581	0.620	0.623	0.484
1592	0.638	0.657	2.978
1597	0.687	0.672	2.183
1610	0.708	0.711	0.424
1618	0.718	0.719	0.139
1620	0.720	0.721	0.139
Average Error (%)			**6.286**

Chapter 4

Design and Analysis of Semi-Elliptical Nano-plasmonic Coupler

4.1 Overview

In this section, design and analysis of a highly efficient three-dimensional nano-plasmonic semi-elliptical coupler between a dielectric waveguide and metal-dielectric-metal (MDM) plasmonic waveguides has been demonstrated. Numerical simulation yields coupling efficiency up to ∼78% at the optical communication wavelength of 1550 nm. The dependence of coupling efficiency has been studied by changing the width of the plasmonic waveguide and the length of the semi-minor axis. Based on these results, the optimum dimensions of the semi-elliptical coupler have been determined. In both scenario, the transmission response of the proposed structure is found to be broadband. Using optimum dimensions, we have analyzed coupling efficiency, reflection coefficient, return loss and voltage standing wave ratio (VSWR) at a broad range of input signal wavelengths.

4.2 Defining Structure

A three-dimensional semi-elliptical dielectric waveguide has been considered in conjunction with a metal-dielectric-metal plasmonic waveguide. The schematic of the proposed structure is presented in Figure 4.1. The width of the dielectric (silicon) has been choosen as 300 nm with reference to the analysis made by G. Veronis *et al.* [5]. The height is taken as 300 nm. The coupler is a semi-elliptical structure with semi-minor axis length defined by parameter a. The width of the plasmonic waveguide is defined by the parameter w_p. Numerical simulations have been performed by varying first a, and then w_p, in order to determine its impact on the coupling efficiency.

The general form of an ellipse can be expressed with the following equation,
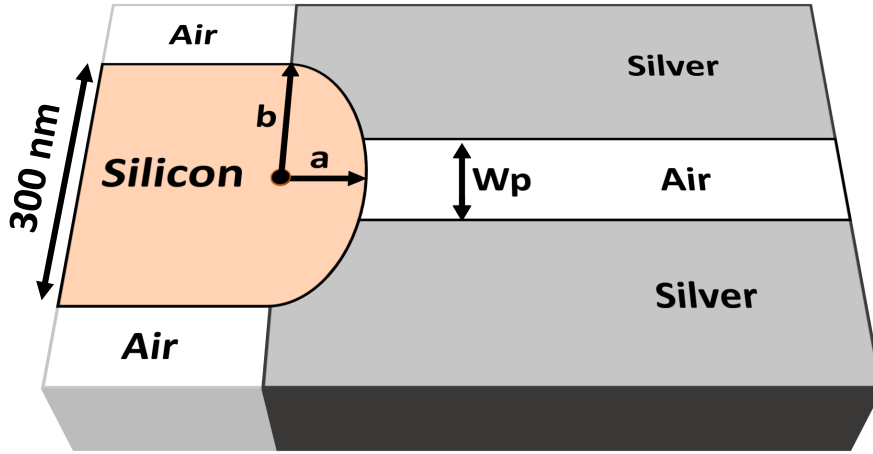
Figure 4.1: Three dimensional view of the semi-elliptical coupling structure

$$\frac{x^2}{a^2} + \frac{y^2}{b^2} = 1 \qquad (4.1)$$

where, a is the semi-minor axis, b is the semi-major axis and $b > a$. We kept b fixed at 150 nm and varied a to find the optimum coupling efficiency.

4.3 Defining Materials

Silver is used as metal and air as the plasmonic waveguide. Dispersive properties of silver have been taken into consideration in our simulation. Silicon is used as the dielectric waveguide which couples light into the MDM subwavelength plasmonic waveguide.

4.4 Method of Analysis

Finite integration technique (FIT) [102] has been used to theoretically investigate the properties of the proposed coupler using 3D electromagnetic (EM) simulation software, CST MWS time domain solver. This allows the use of experimental data directly when the dielectric constant of metals (such as silver) is dependent on frequency [12]. At every boundary of the simulation domain, perfectly matched layer (PML) is used [114] by keeping all the boundaries open in CST MWS. This is done to prevent back reflections by attenuating fields within the boundary regions. Both the waveguides (i.e. dielectric and MDM waveguide) are aligned with their axes. To calculate the coupling efficiency, transmission and reflection coefficients, and other performance parameters, the fundamental mode is excited at the input waveguide and the power is measured at both the dielectric (input) and plasmonic (output) waveguides

through different ports.

Power transmitted into the MDM plasmonic waveguide is measured just after the interface of the two waveguides with MDM waveguide being the output waveguide. While measuring the power from dielectric waveguide side, it has been ensured that measurements have been taken from the interface of both waveguides in such a way that negligible contribution of radiative modes in the measured power has been considered [5].

G. Veronis *et al.* [5] has proposed a structure having 300 nm silicon dielectric waveguide and 40 nm air plasmonic waveguide. Light is coupled from the dielectric waveguide into the MDM plasmonic waveguide. To validate our results, we have simulated this structure and obtained the same coupling efficiency of 68% at 1550 nm, which can be observed in Figure 4.2 and 4.3 for $a = 0$ nm.

Coupling efficiency has been defined as the ratio of the power incident at the MDM
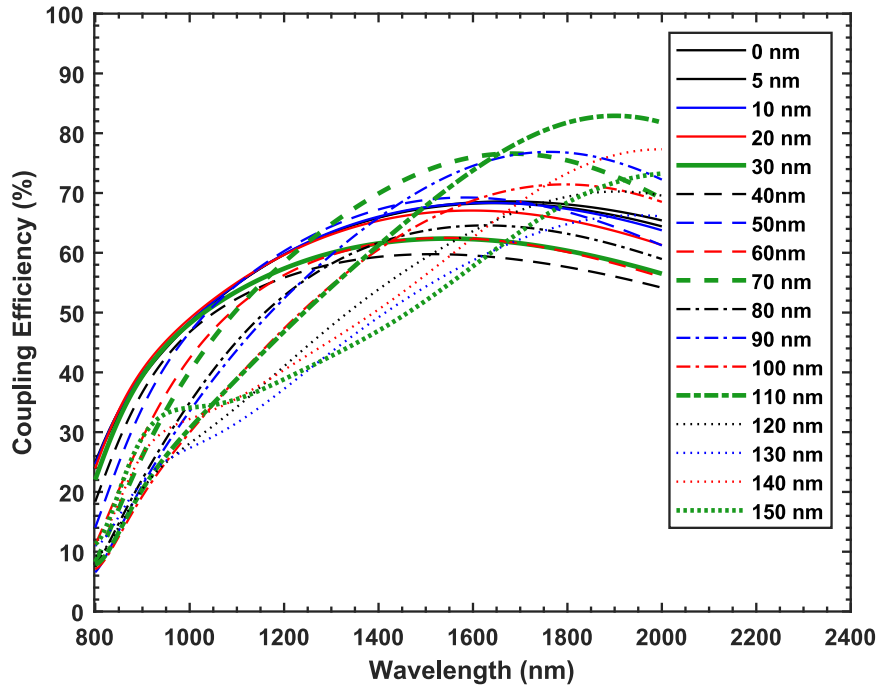
Figure 4.2: Coupling Efficiency vs Wavelength

plasmonic waveguide and the power incident at the silicon waveguide. With this definition, the ports have been assigned. *Port i* connected to the silicon waveguide excites power, which is coupled into the MDM plasmonic waveguide. *Port j*, connected at the onset of the MDM plasmonic waveguide measures the power incident on it. Then the reflection coefficient can be determined by the formula [115],

$$\rho = \sqrt{\frac{P_j}{P_i}} \tag{4.2}$$

31
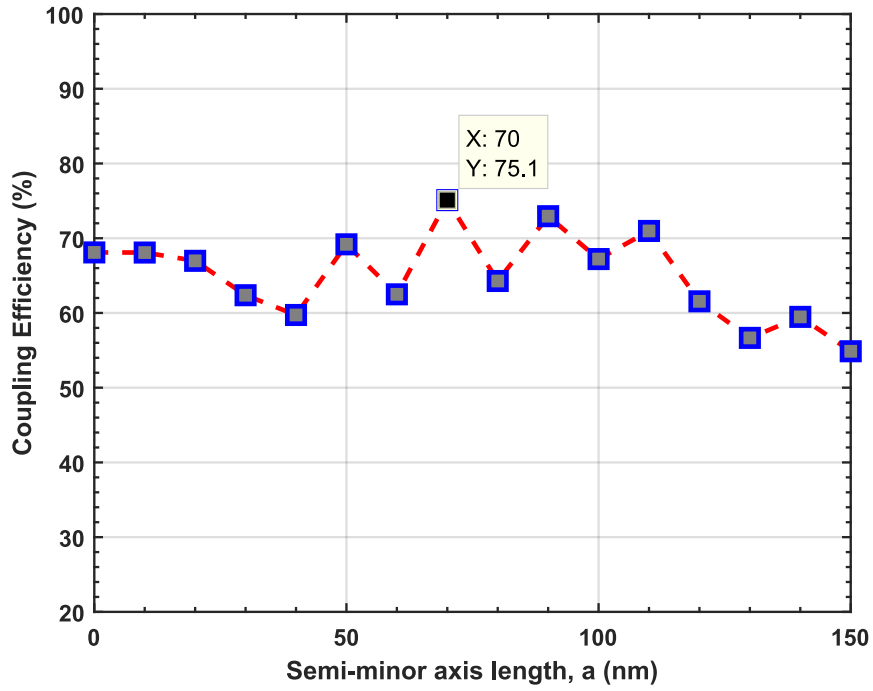
Figure 4.3: Coupling Efficiency vs Semi-minor axis length
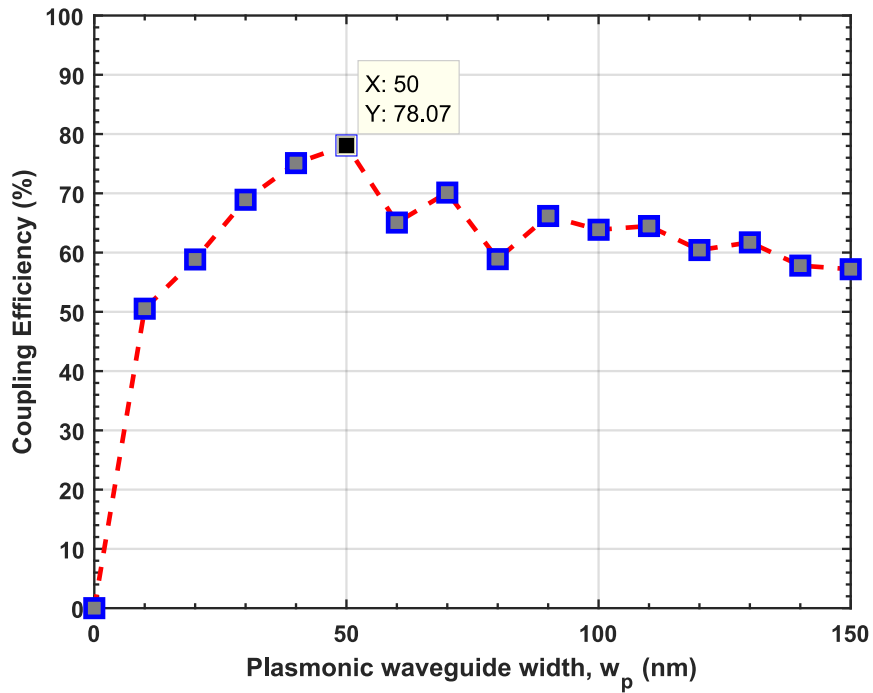
Figure 4.4: Coupling Efficiency vs Plasmonic Waveguide Width

where, P_j is the power incident on *Port j* and P_i is the power injected into the Si waveguide through *Port i*.
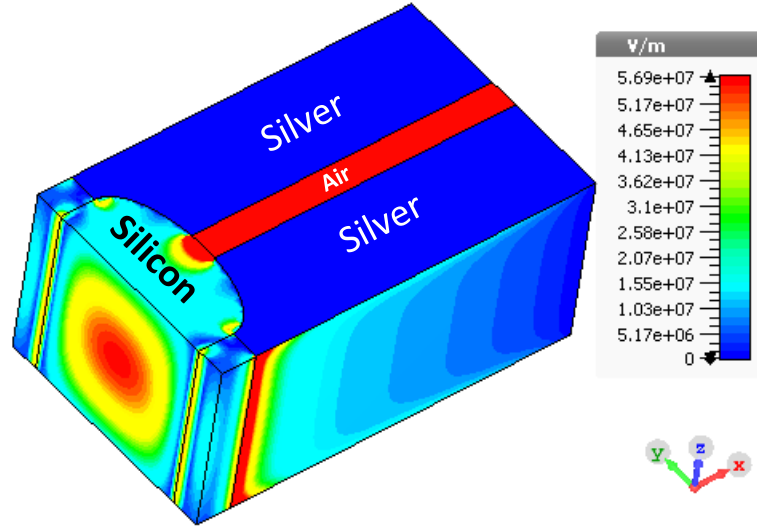
Figure 4.5: Electric field distribution at communication wavelength (1550 nm)

Table 4.1: Value of the simulation parameters at optical communication wavelength (1550 nm)

Parameters	Value
Transmitted Power	0.7805
Reflected Power	0.1413
Absorbed Power	0.0782
Reflection Coefficient Magnitude	0.3748
Return Loss	8.523 dB
VSWR	2.199
Mismatch Loss	0.6575 dB

From the value of the reflection coefficient, VSWR, return loss (in dB) and mismatch loss can be determined using the following formulas [115].

$$VSWR = \sqrt{\frac{1+\rho}{1-\rho}} \tag{4.3}$$

$$RL_{dB} = -20 \log \rho \tag{4.4}$$

$$ML_{dB} = -10 \log(1-\rho^2) \tag{4.5}$$
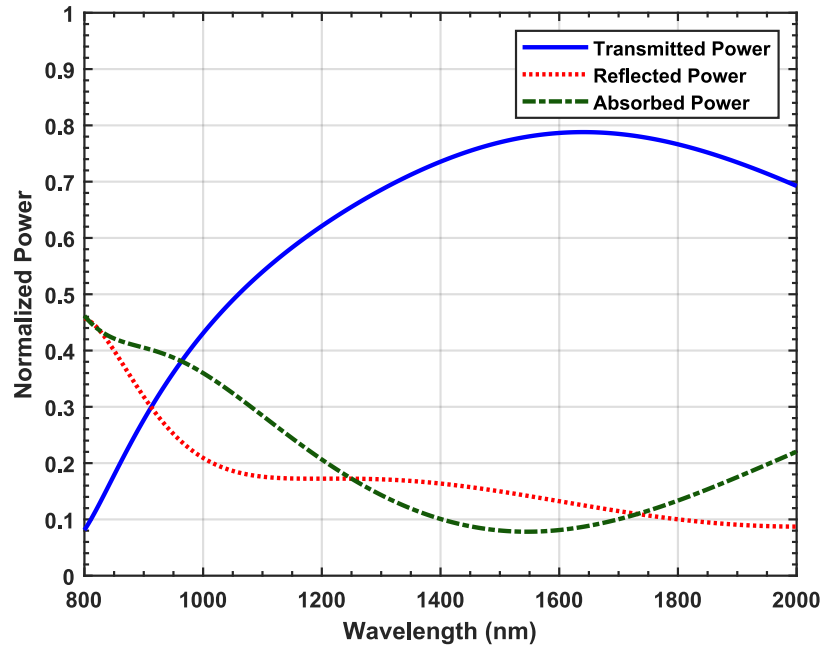
(a)
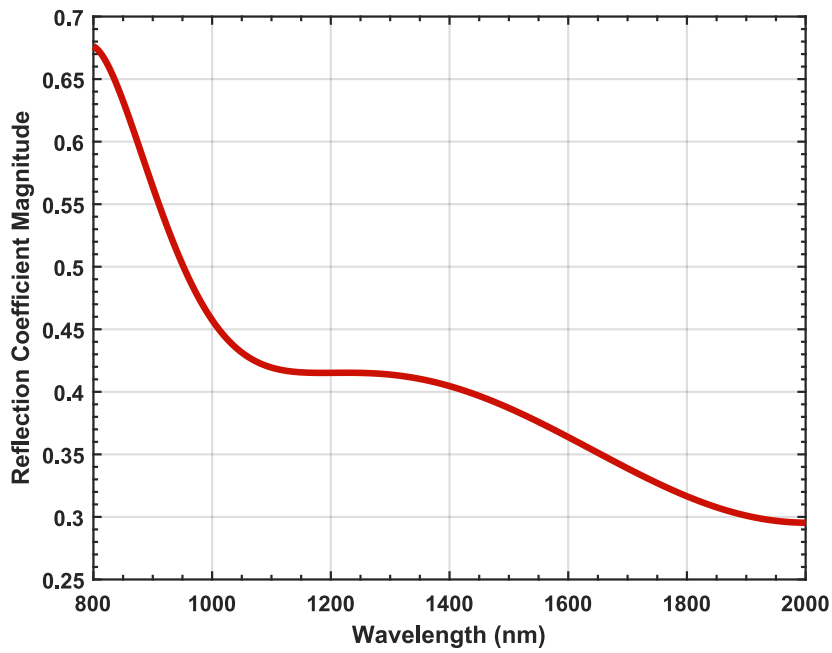
(b)

Figure 4.6: Simulation results of different performance parameters for the semi-elliptical coupler having optimum dimensions ($w_p = 50$ nm and $a = 70$ nm) as a function of wavelength. (a) normalized power. (b) reflection coefficient magnitude.

4.5 Results and Discussions

Keeping the optimum dimensions determined by G. Veronis *et al.* [5] (i.e. $w_p = 40$ nm and Si Waveguide $width = 300$ nm), the semi-minor axis length a has been varied

(a)

(b)

Figure 4.7: Simulation results of different performance parameters for the semi-elliptical coupler having optimum dimensions ($w_p = 50$ nm and $a = 70$ nm) as a function of wave-length.(a) VSWR.(b) return loss.

from 0 nm (same as rectangular dielectric waveguide) to 150 nm (semicircle). The coupling efficiency has been calculated for these dimensions and presented in Figure 4.2.

The coupling efficiency at the optical communication wavelength (1550 nm) as a

function of corresponding semi-minor axis length a is shown in Figure 4.3. From this

(a)
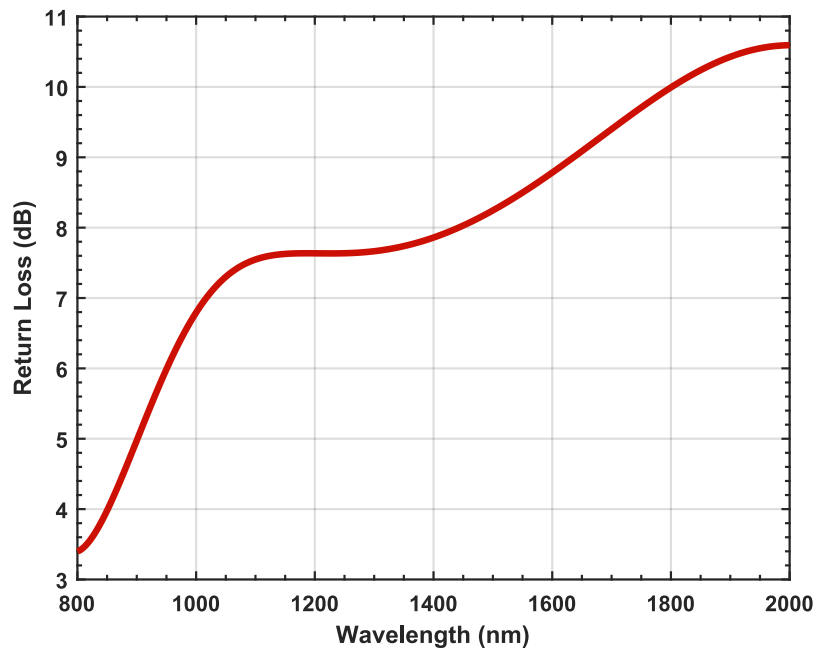
(b)

Figure 4.8: Simulation results of different performance parameters for the semi-elliptical coupler having optimum dimensions ($w_p = 50$ nm and $a = 70$ nm) as a function of wavelength.(a) VSWR.(b) return loss.

figure, we observe that the coupling efficiency at first decreases as a is increased and the maximum value is obtained at $a = 70$ nm. Now keeping a as 70 nm, we have varied the width of the plasmonic waveguide, w_p, from 0 nm to 150 nm. The analysis

is presented in Figure 4.4.

In Figure 4.4, we observe that, when w_p is 0 nm, efficiency is 0, which is expected. The coupling efficiency increases as the width of the air region of MDM waveguide, w_p, increases up to 50 nm, and then it starts decreasing. Thus, we have obtained the optimum dimensions for maximum coupling efficiency (about 78%) for our proposed structure at $a = 70$ nm and $w_p = 50$ nm.

The electric field distribution at optical communication wavelength (1550 nm) of the coupling structure of Figure 4.1 has been presented in Figure 4.5. From the color map

of the figure, the field intensity can be observed to be much lower in the metallic layer than the dielectric side of plasmonic waveguide because of higher loss component in the metallic layer. As such, the optical mode is strongly confined to the subwavelength core of the waveguide on account of the coupling configuration.

Furthermore, with these dimensions, we simulate the structure to investigate the coupling efficiency, reflection coefficient, VSWR, return loss and mismatch loss at different input signal wavelengths. In all cases, the transmission response of our proposed structure is found to be broadband. The analysis is shown in Figure 4.8.
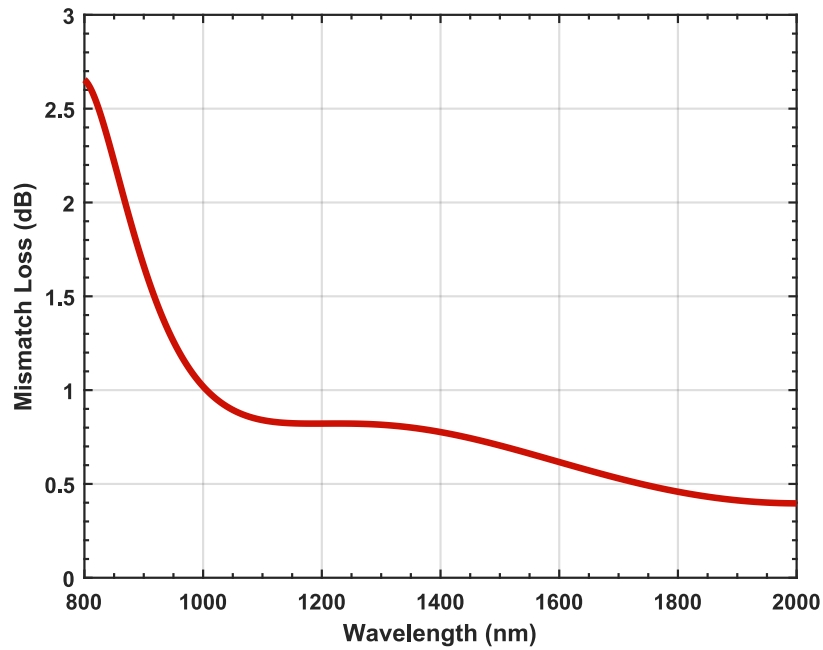
(a)

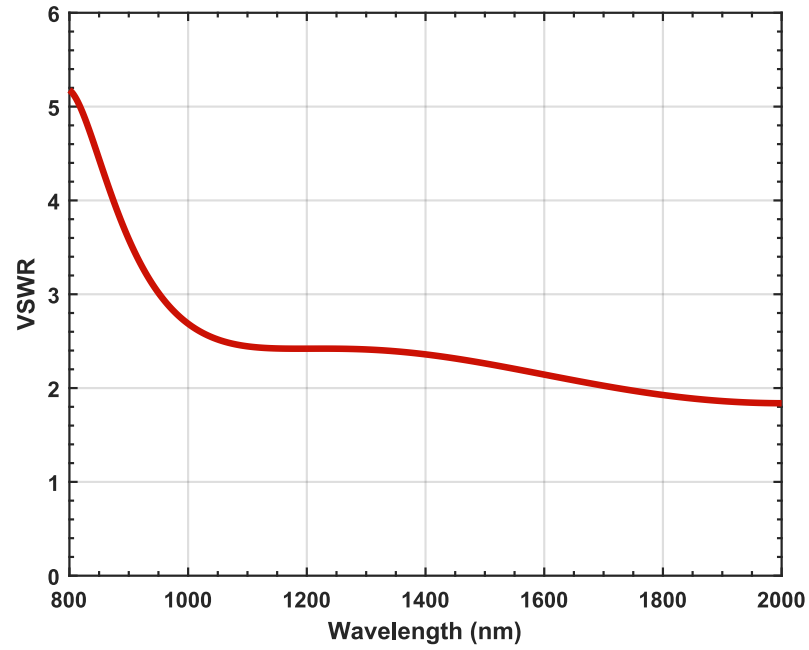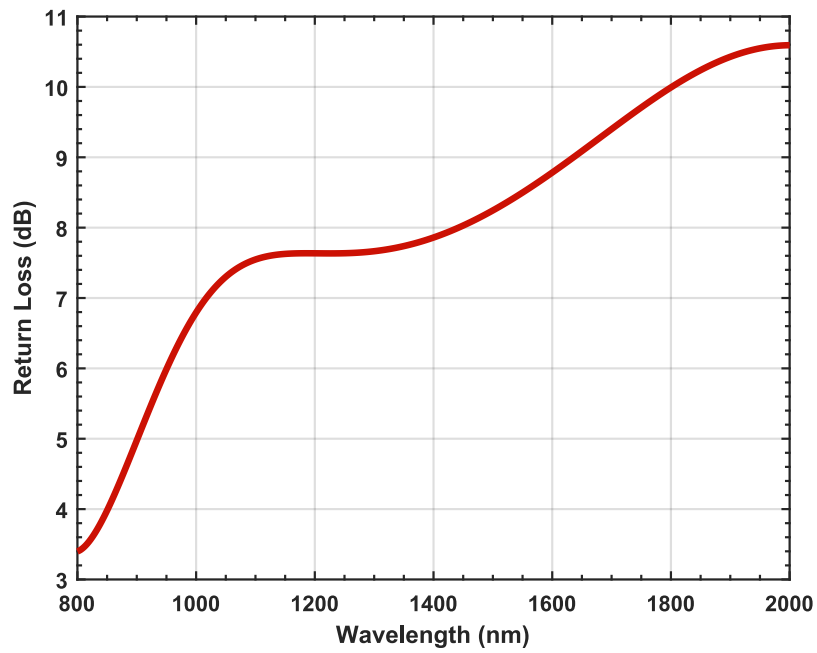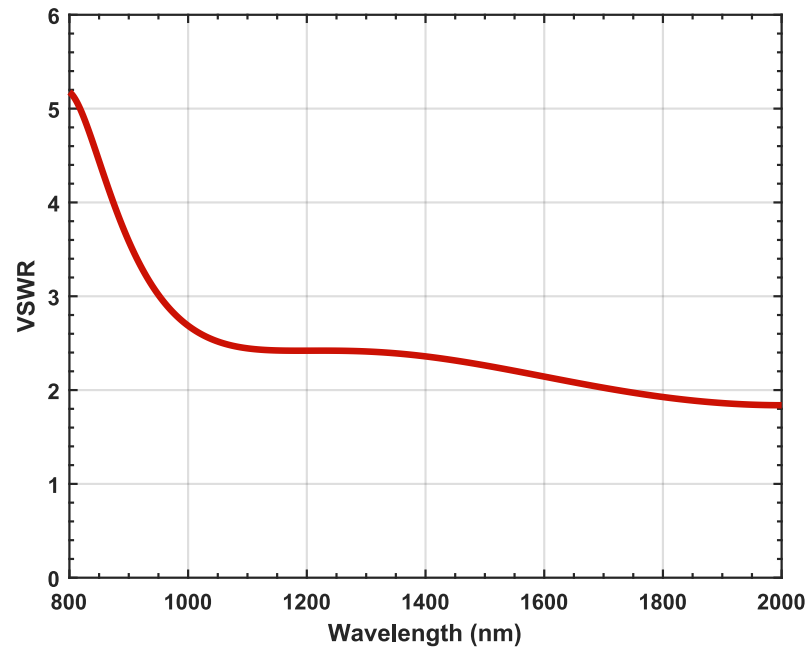**Figure 4.9:** Simulation results of different performance parameters for the semi-elliptical coupler having optimum dimensions ($w_p = 50$ nm and $a = 70$ nm) as a function of wavelength.(a) mismatch loss

For the optimal dimension at communication wavelength, the coupling efficiency

is found to be 78% in Figure 4.8(a). The values of different performance parameters at the optical communication wavelength (1550 nm) has been presented in Table 4.1. We observe that sum of the transmitted, reflected and absorbed power constitute 1.0, which is expected. The reflection coefficient is found to be 0.3834 in Figure 4.8(b) which indicates tolerable reflection. From Figure 4.8(c), VSWR is close to 2.0 which is small enough since the smaller the VSWR is, the better the device, and the more power is delivered (minimum VSWR is 1.0). From Figure 4.8(d) Return loss is also found to be comparatively high ($\sim$8 dB), indicating lower impedance mismatch at this wavelength. In Figure 4.8(e), the mismatch loss is found to be low ($\sim$ 0.66 dB), indicating power wastage due to reflection and impedance mismatch [116].

4.6   Advantages of Semi-Elliptical Plasmonic Coupler

There are some advantages of a simple semi-elliptical nanoplasmonic coupler over any other already proposed plasmonic couplers. They have been mention below:

1. Simple semi-elliptical nanoplasmonic coupler has a better coupling efficiency than that of the many other already proposed plasmonic couplers, especially, rectangular plasmonic couplers.

2. The semi-elliptical nanoplasmonic coupler can operate at a broad range of frequencies. It can operate at a satisfactory level around the telecommunication wavelength of 1550 nm.

3. Besides, this coupler can perform better when performance parameters like VSWR, reflectance, absorbance, etc. will be considered. Its performance is far better than the rectangular plasmonic couplers which have been proposed so far.

4. Due to its being simple in structure, a simple semi-elliptical nanoplasmonic coupler can be fabricated very easily.

Chapter 5

Design and Analysis of Air Gap–Based Semi-Elliptical Nanoplasmonic Coupler

5.1   Overview

Efficient coupling of light between the dielectric waveguide and plasmonic waveguide has been investigated theoretically in three dimensions. An air gap-based novel nanoplasmonic semi-elliptical structure of silicon (Si) is used as a coupler, which connects these waveguides. Finite integration technique (FIT) has been deployed for the investigation. Theoretical coupling efficiency of $\sim$85% near the optical communication wavelength (1550 nm) has been achieved through numerical simulations. The dependency of coupling efficiency has been investigated by varying the curvature of the semi-elliptical coupler, the air gap width between the two waveguides and the width of the air gap of silver-air-silver waveguide, and an optimal dimension of the proposed structure has been determined. A number of performance parameters like coupling efficiency, reflection coefficient, return loss, and voltage standing wave ratio (VSWR) have been analyzed with the obtained optimal dimensions. Broad range of operating frequency, tolerance to coupler thickness, angular, and air gap misalignment, and excellent agreement to a demonstrated experimental coupler has made the proposed coupler distinctive.

5.2   Defining Structure

An air gap based semi-elliptical coupler in three-dimension has been considered for coupling the dielectric waveguide with a metal-dielectric-metal (MDM) plasmonic waveguide. The MDM plasmonic waveguide is formed after sandwiching air (insulator) in between two silver (metal) plates. The geometry designated with the labels of the proposed structure is shown in Figure 5.1.

The width of the Si coupler is taken as 300 nm as per the analysis made by G.
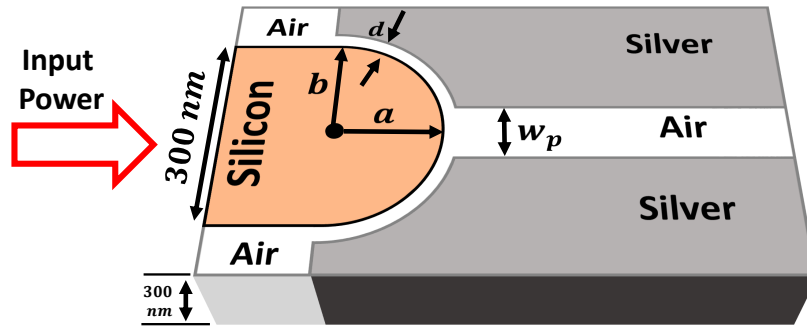
Figure 5.1: Three dimensional view of the proposed air gap based semi-elliptical nano-plasmonic coupler.

Veronis *et al.* [5]. The height of both the Si and plasmonic waveguide is taken as 300 nm. The width of the air gap between the metals of the plasmonic waveguide is represented by w_p, whereas the width of the air gap between the two waveguides is represented by d, as shown in Figure 5.1. The semi-elliptical coupling structure has a semi-minor axis and a semi-major axis, lengths of which are defined by the parameters a and b. The relationship between these two parameters can respectively be obtained from the general expression of an ellipse, denoted by the following equation.

(a) $a = 0$ nm

(b) $a = 50$ nm

(c) $a = 110$ nm

(d) $a = 150$ nm
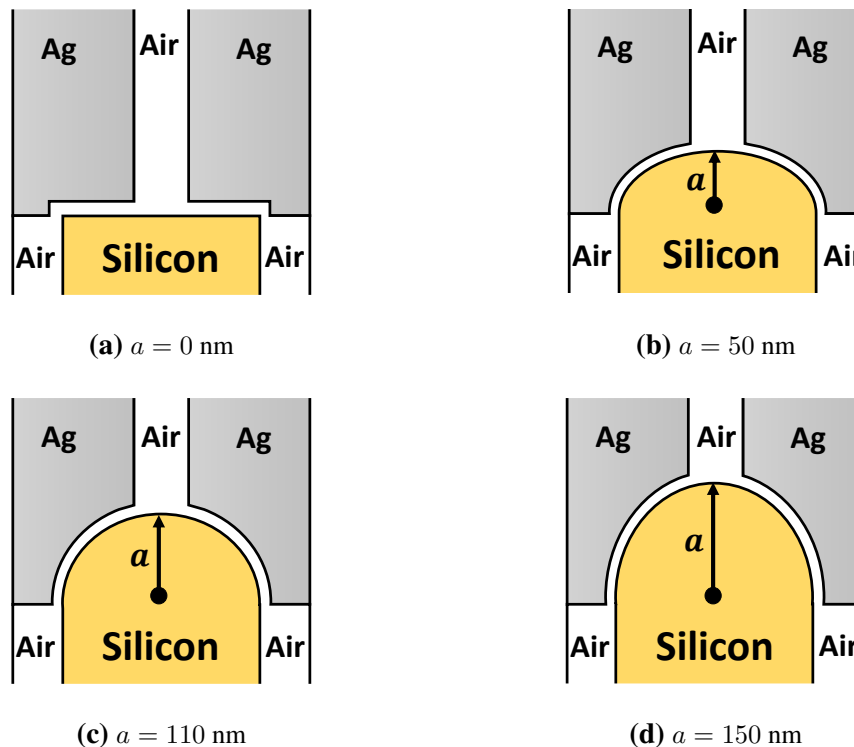
Figure 5.2: Top view of the nano-plasmonic coupler showing variation of the semi-minor axis length, a, that is used in simulation

$$\frac{x^2}{a^2} + \frac{y^2}{b^2} = 1, \tag{5.1}$$

where, semi-minor axis length, a, is less than the semi-major axis length, b. Length of b is kept fixed at 150 nm for all different simulations. Our main point of interest among all different parameters are the semi-minor axis length (a), width of the air gap between the two waveguides (d) and width of the air gap between the metals of the plasmonic waveguide (w_p). By observing the variation of coupling efficiency with all of these parameters, the optimal dimensions of the coupling structure is obtained. Silicon is used in the coupling structure to couple light into the MDM subwavelength plasmonic waveguide from the dielectric waveguide.

5.3   Defining Materials

Silicon has been chosen as the material for the dielectric waveguide. For the metal-dielectric-metal (MDM) plasmonic waveguide, silver has been chosen as the metal, and air has been selected as the dielectric material.

5.4   Obtaining Optimal Dimensions

With a view to obtaining the optimal semi-minor axis length (a) of the semi-elliptical structure, we varied a from 0 nm (vertical line) to 150 nm (semi-circle) with 10 nm step size. The coupling structure for four different values of a is shown in Figure 5.2. Figure 5.3(a) shows the coupling efficiency within the wavelength range of 800 nm to 2200 nm for different values of a. Coupling efficiency at optical communication wavelength (1550 nm) has been plotted against a in Figure 5.3(b).

Table 5.1: Summary of dimensions of the optimized nano-plasmonic coupler

Dimension	Value
Semi-minor axis length, a	110 nm
Air gap width, d	5 nm
Width of the plasmonic waveguide, w_p	50 nm

Analyzing Figure 5.3(b), we observe that the coupling efficiency is maximum ($\sim$83%) at the optical communication wavelength (1550 nm) at a semi-minor axis length, $a = 110$ nm. After that, an optimized air gap between the two waveguides (i.e. d) has been determined by varying d from 0 nm (neglecting air gap) to 50 nm with 5 nm
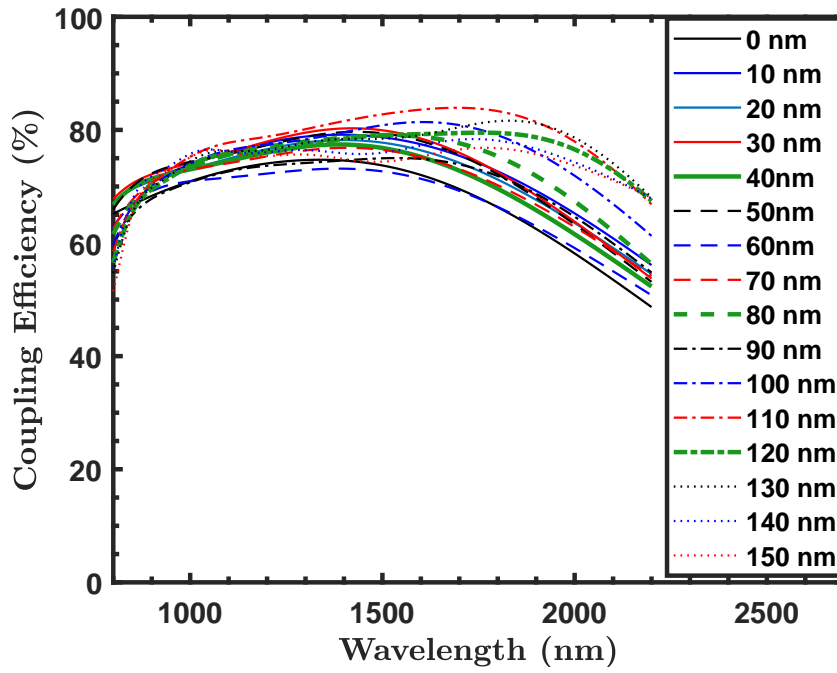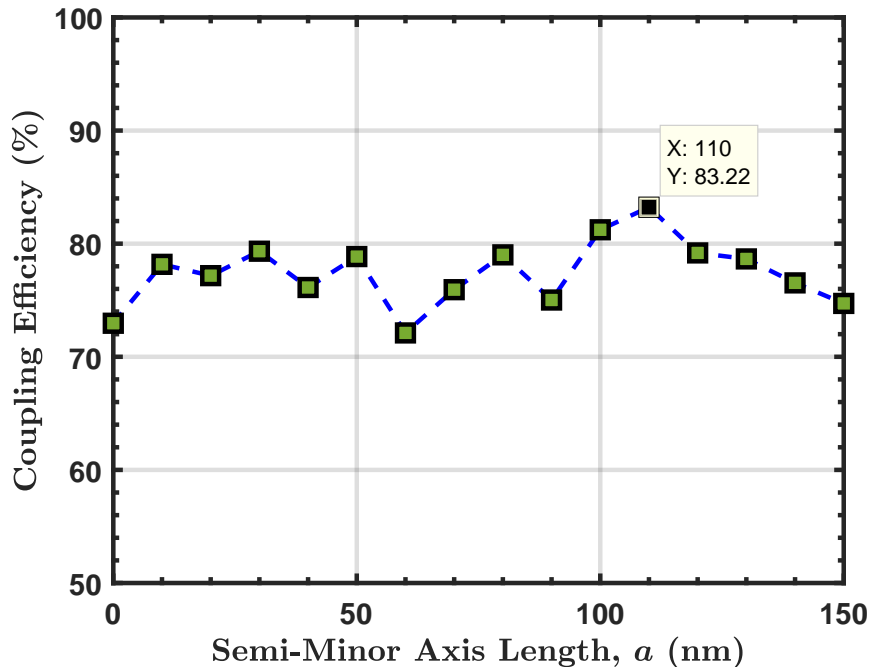
Figure 5.3: Variation in coupling efficiency (a) with varying wavelength and (b) with varying semi-minor axis length, a, at 1550 nm.

step size and observing the corresponding coupling efficiency. The optimum value of d is obtained from the analysis of coupling efficiency as a function of air gap between the two waveguides as observed in Figure 5.4(a).

From Figure 5.4(a), it is seen that only air gap of width 5 nm in between the two waveguides provides maximum coupling efficiency of ∼83%. Thus, the optimum
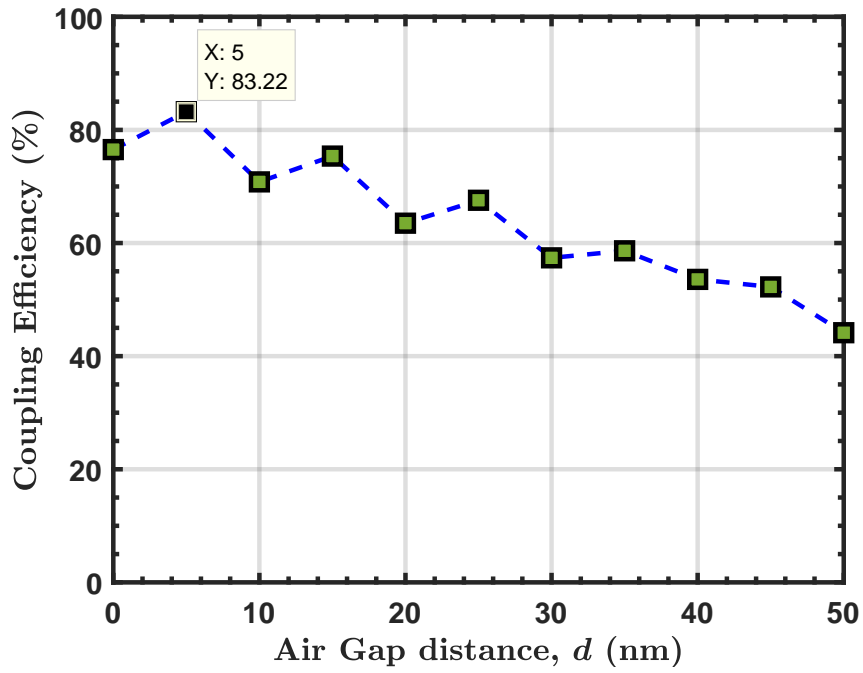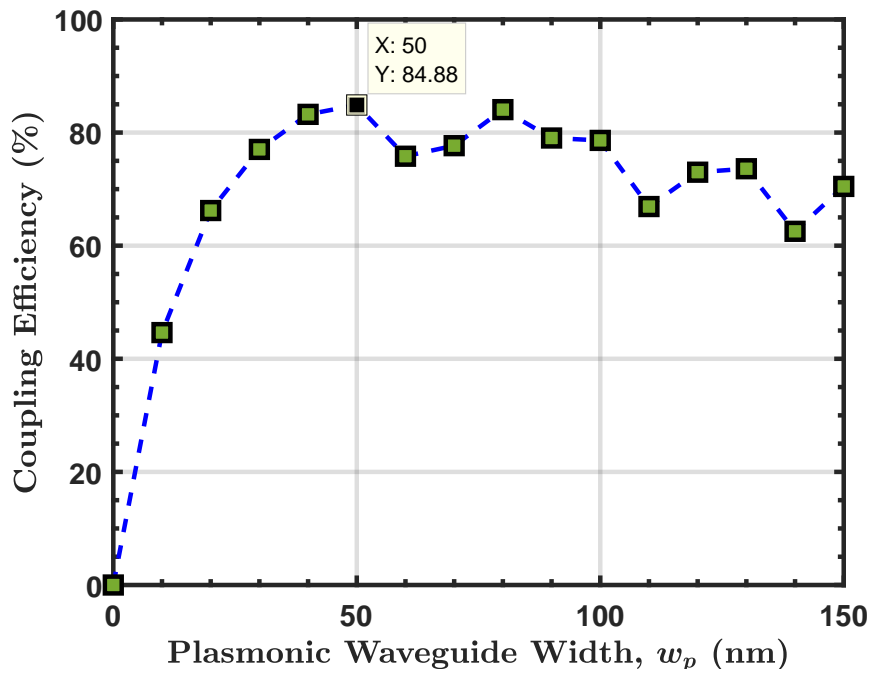
Figure 5.4: Variation of coupling efficiency at the optical communication wavelength (1550 nm) (a) with varying air gap distance between the dielectric and plasmonic waveguide, d and (b) with varying width of the air gap between the metals of the plasmonic waveguide, w_p.

value of d is 5 nm. To get the optimum width of the air gap between the metals of the plasmonic waveguide, w_p is varied from 0 nm to 150 nm with 10 nm step size and the corresponding coupling efficiency is recorded. From the plot of coupling efficiency vs width of the air gap between the metals of the plasmonic waveguide (i.e. w_p) de-

picted in Figure 5.4(b), we get 50 nm as the optimum value of w_p. The dimensions of the optimized coupler yielding maximum coupling efficiency is presented in table 5.1.

5.5 Performance of the Optimized Coupler

Using the optimal dimensions demonstrated in Table 5.1, the proposed nano-plasmonic semi-elliptical coupler has been simulated to obtain different performance parameters such as normalized power, coupling efficiency, reflection coefficient, return loss, and VSWR for a wavelength range of 800 nm to 2000 nm.
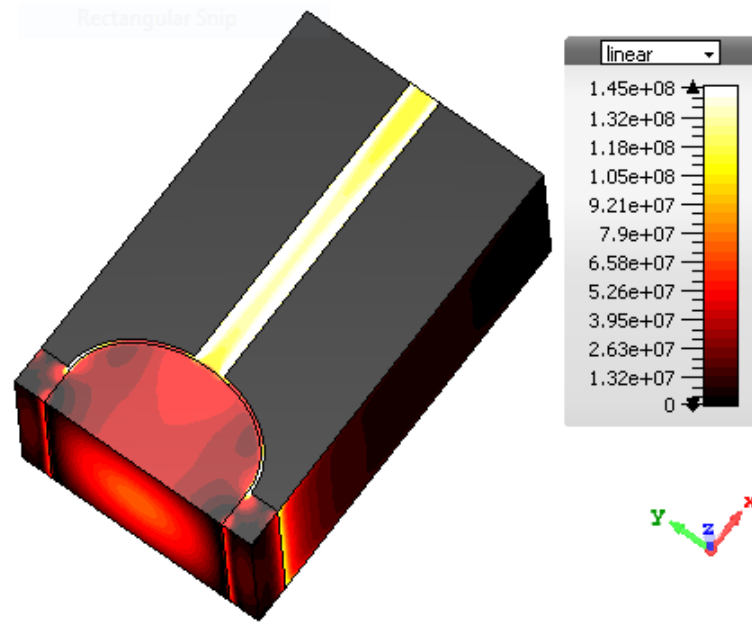
Figure 5.5: A three dimensional view of the structure showing the electric field profile (E_y) at 1550 nm

Section 5.5 shows the electric field distribution at the communication wavelength (1550 nm). Colorimetric change with respect to the electric field and x, y, and z directions are shown on the inset. It also gives a visual perception of how efficient the proposed coupler is in terms of coupling. Figure 5.6 shows the variation of normalized transmitted power, reflected power and absorbed power with the wavelength. At 1550 nm, we have found normalized reflectance (~ 0.056) and absorbance (~ 0.095) to be very small. On the other hand, the obtained normalized transmittance (~ 0.849) is found to be much large. The spatial plot of normalized $|E_y|$ field profile along y-axis is demonstrated in Figure Figure 5.7, which shows high plasmon confinement at the interface of the dielectric waveguide (air) and metal (Ag). We also observe that the attenuation of the field profile at the central part of the dielectric waveguide due to dielectric loss is small.
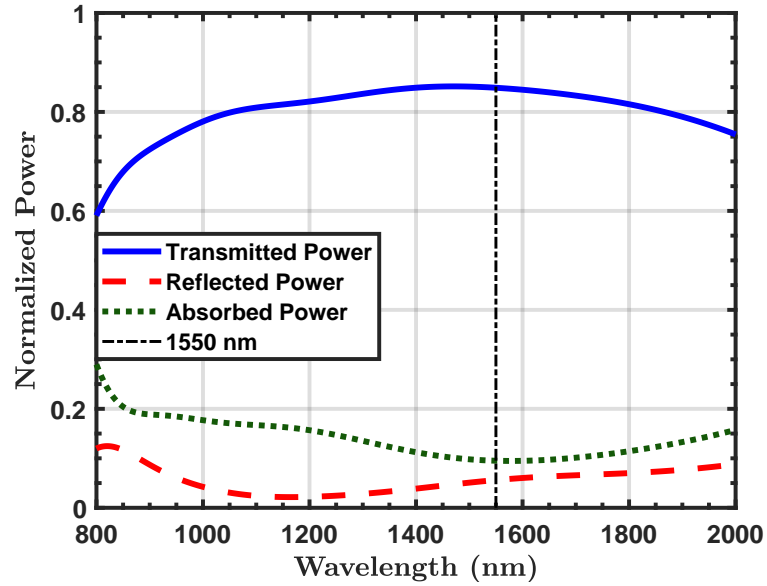
Figure 5.6: Variation of normalized transmitted power, reflected power, and absorbed power with respect to wavelength.

Figure 5.8(a) shows the coupling efficiency variation with the change of wavelength from 600 nm to 2200 nm. The coupling efficiency near the optical communication wavelength (1550 nm) for the proposed coupler has been found to be ~85%. It is also observed that the coupling efficiency is considerably large for a broad range of wavelengths. It is above 80% from 1010 nm to 1810 nm. Figure 5.8(b) shows the reflection coefficient variation with the change of wavelength. A reflection coefficient of ~ 0.24 is found at 1550 nm.

Figure 5.9(a) shows the return loss variation with the change of wavelength. At 1550 nm, the value of the return loss is found to be 12.51 dB, which is more than the minimum acceptable value of the return loss (typically 10 dB). The obtained return
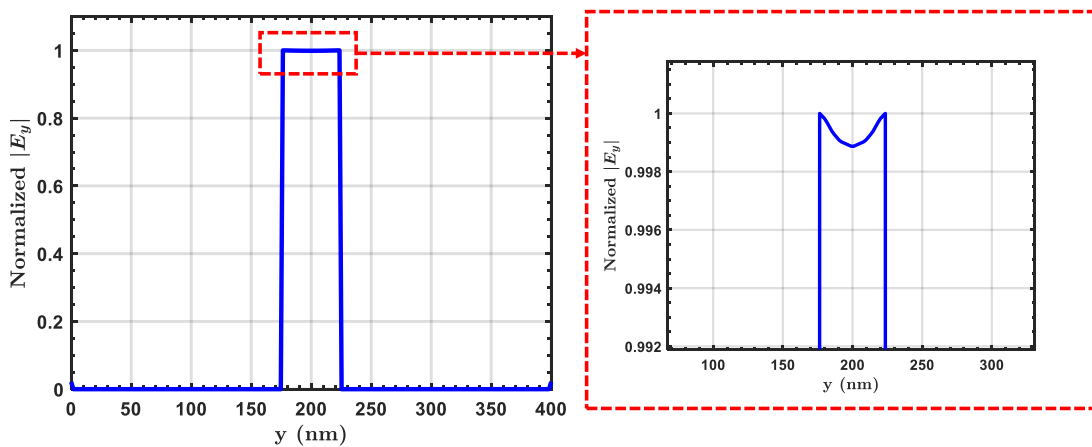
Figure 5.7: Spatial plot of the magnitude of the normalized E_y field profile at a length and height of 200 nm and 150 nm respectively
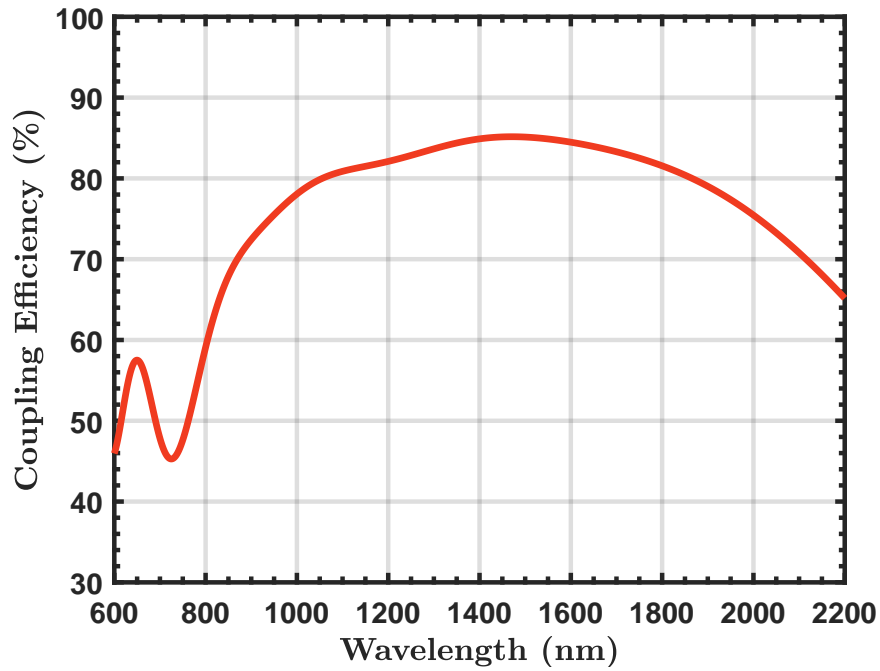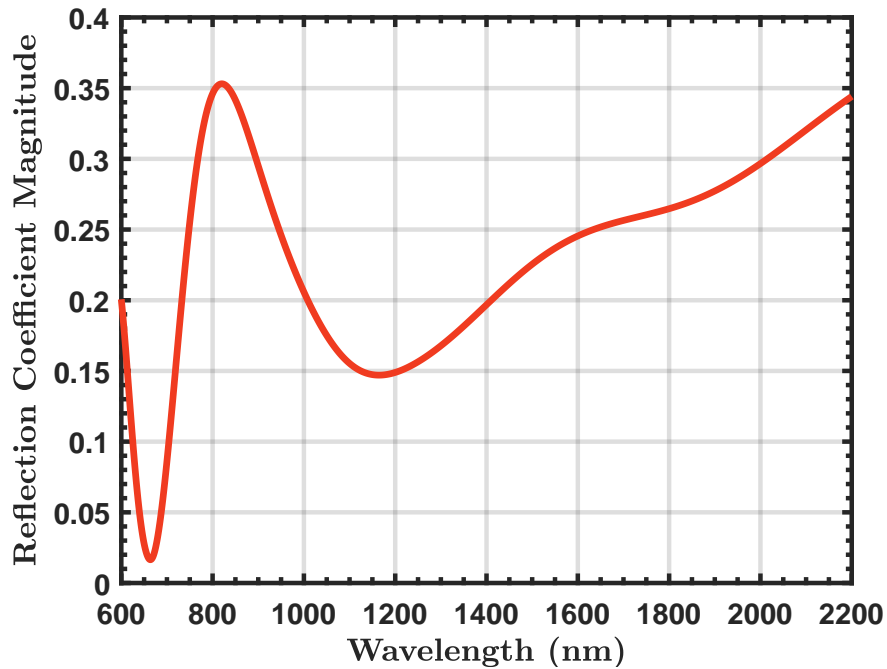
Figure 5.8: Analysis of different performance parameters as a function of wavelength (a) coupling efficiency (%), (b) magnitude of reflection coefficient.

loss indicates lower impedance mismatch at the optical communication wavelength. Figure 5.9(b) shows the VSWR variation with the change of wavelength. At 1550 nm, the value of the VSWR is found to be ~ 1.624 which is acceptable as it is less than 2.0. Since, smaller the value of VSWR, the more the power is delivered (minimum value of VSWR is 1.0). The values of different performance parameters at the communication
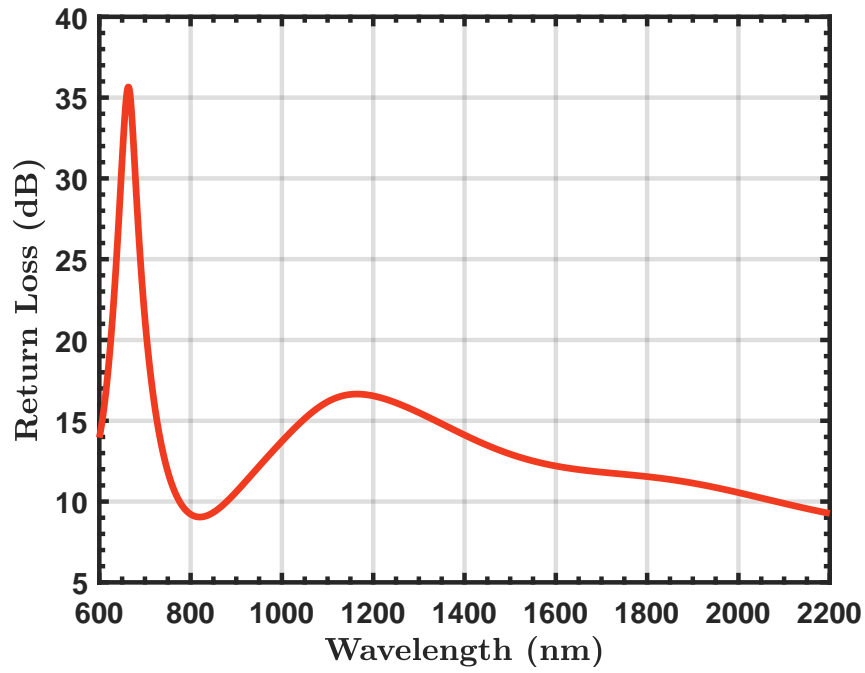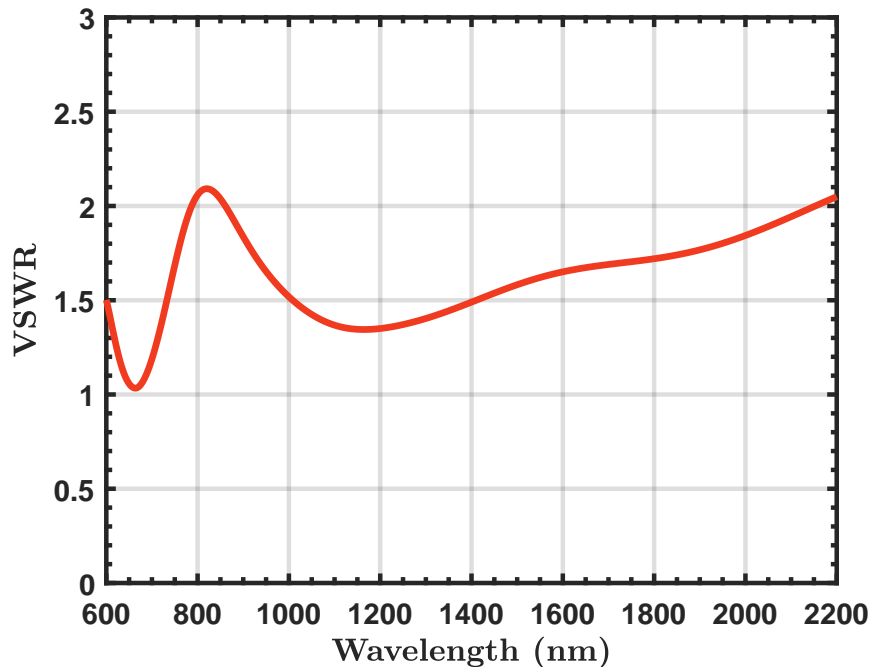
Figure 5.9: Analysis of different performance parameters as a function of wavelength (a) return loss (dB), and (b) VSWR.

wavelength (1550 nm) is summarized in table 5.2.

Different nano-plasmonic couplers have been proposed over the years. The rectangular coupler proposed by Veronis *et al.* [5] has a theoretical transmission efficiency of ∼70%. A multi-section tapered coupler has also been proposed in [5] having a trans-

Table 5.2: Summary of different performance parameters of the optimized nano-plasmonic coupler at 1550nm.

Performance Parameter	Value
Transmittance	0.8488
Reflectance	0.0561
Absorbance	0.0951
Reflection Coefficient Magnitude	0.237
Return Loss	12.51 dB
VSWR	1.624

mission efficiency of ∼93%, however, it has the disadvantage of fabrication related complexity. Rectangular couplers with different dielectric material have been investigated in [10, 117, 118], all of them having coupling efficiency below 70%, whereas our proposed optimized nano-plasmonic coupler, with flexibility in fabrication, has an efficiency of ∼85%.

5.6 Tolerance to Angular, Air Gap, and Coupler Thickness Misalignment

Consideration of alignment accuracy and resolution of different lithographic processes [119] is important for the fabrication of plasmonic waveguides in nano scale. Consequently, analyzing the tolerance limit of the key performance parameters of the nano-plasmonic coupler has become essential. Here, we have observed the impact of angular and air-gap misalignment on the coupling efficiency of the semi-elliptical coupler.
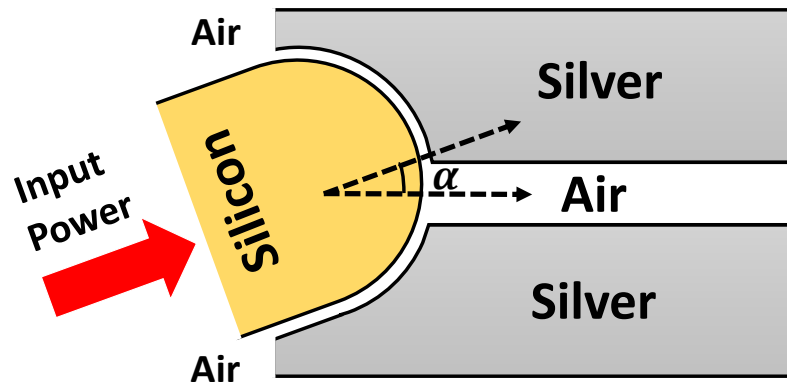
Figure 5.10: Angular misalignment (top view) between the axis of two couplers defined by the parameter α.

First, the angular alignment has been varied from $0°$ to $\pm5°$ and it is found to give coupling efficiency above 77% and the values are summarized in table 5.3. Figure 5.10 shows the schematic when angular misalignment is considered, and α represents

Table 5.3: Tolerance limit of angular misalignment and value of coupling efficiency at 1550 nm.

Angular Alignment	Value
0° (no misalignment)	84.88%
+5°	78.20%
−5°	77.00%
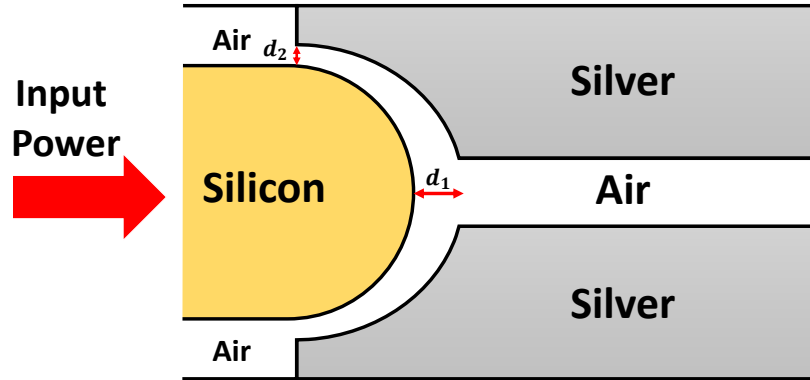
Figure 5.11: Top view of the air gap misalignment between the axis of two couplers defined by d_1 and d_2.

the angular shift that the coupler has undergone from horizontal alignment during the fabrication process.

Table 5.4: Tolerance limit of air gap misalignment and value of coupling efficiency at 1550 nm.

Air Gap Alignment	Value
$d_1 = d_2$	84.88%
$d_1 > d_2$	76.50%
$d_1 < d_2$	71.20%

Tolerance to air gap misalignment between the two waveguides (d) is depicted in Figure 5.11. We have considered the situation when the air gap between the two waveguides, d, is not uniform (i.e. $d_1 \neq d_2$). Three cases are analyzed; when there is no misalignment (i.e. $d_1 = d_2$), when there is a horizontal shift in d_1 by 10 nm (i.e. $d_1 > d_2$), and when there is a vertical shift in d_2 by 10 nm (i.e. $d_1 < d_2$). The corresponding tolerance limit is demonstrated in table 5.4.

5.7 Advantages of Air Gap-Based Semi-Elliptical Nanoplasmonic Coupler

There are some advantages of air gap-based semi-elliptical nanoplasmonic coupler over any other proposed plasmonic couplers. They have been mention below:

1. Air gap-based semi-elliptical nanoplasmonic coupler has a better coupling efficiency than that of the simple semi-elliptical nanoplasmonic coupler and many other already proposed plasmonic couplers.

2. It has the capability to tolerate the angular misalignment as well as air gap misalignment between the waveguides. This was was not available in the simple semi-elliptical nanoplasmonic coupler mentioned in Chapter 4. Besides, to the best of the author's knowledge, this feature is not available in the maximum of the already proposed couplers.

3. The air gap-based semi-elliptical nanoplasmonic coupler has the ability to operate at a broad range of frequencies. It can operate at a satisfactory level around the telecommunication wavelength of 1550 nm.

4. Besides, this coupler can perform better when performance parameters like VSWR, reflectance, absorbance, etc. will be considered. Its performance is far better than the rectangular plasmonic couplers which have been proposed so far.

5. Due to its being simple in structure, the air gap-based semi-elliptical nanoplasmonic coupler can be fabricated very easily.

Chapter 6

Conclusion and Future Work

6.1 Conclusion

A novel design of a nanoplasmonic coupling structure with a semi-elliptical shape with or without an air gap in between has been analyzed numerically to justify different performance parameters like coupling efficiency, reflection coefficient, VSWR, and return loss. Optimum dimensions of the coupler have been achieved after varying air gap of the silver-air-silver waveguide, the curvature of semi-elliptical structure, the width of air gap in between the two waveguides (when the air gap is considered), and observing the corresponding coupling efficiency. Optimal dimensions (width of the plasmonic waveguide, a = 50 nm and semi-minor axis length, w_p = 70 nm) were obtained for the case where there will not be any air gap, by varying the dimensions and observing the performance of the coupler. In this case, the proposed coupler yields a coupling efficiency of ∼78% at optical communication wavelength (1550 nm), and the impedance mismatch is also comparatively small. Results show better performance compared to the rectangular waveguide proposed by G. Veronis et al., which has a maximum coupling efficiency of 68%.

For the air gap-based semi-elliptical nanoplasmonic coupler, the optimal structure had a semi-minor axis length (a) of 110 nm, air gap width (d) of 5 nm, and width of the plasmonic waveguide (w_p) of 50 nm. The optimized coupler is capable of providing a coupling efficiency of ∼85% near the optical communication wavelength (1550 nm), which is comparatively higher than many other proposed couplers.

A broad range of operating frequency, acceptable values of return loss, and VSWR, etc. are the distinctive features of the novel designs. Moreover, tolerance to coupler thickness, angular, and air gap misalignment are some of the attractive features of our proposed coupler, which can give flexibility to the fabrication process. The semi-elliptical shape of the coupler augments the distinctive advantage of providing

a comparatively greater coupling surface area for SPP propagation and better phase-matching conditions, thereby yielding higher efficiency than most conventional rectangular couplers. It is expected that the proposed structure along with the analysis will open up new dimensions for efficient plasmonic coupler design.

Table 6.1: Comparison with previous plasmonic couplers

Ref.	Structural design	Efficiency %	Year
[30]	Lateral taper funnel coupler	33%	2010
[31]	Air-Slot coupler Toward Dense Optical ICs	40%	2015
[32]	Slot-to-slot plasmonic coupler	43%	2010
[33]	Slot-to-slot coupling	50%	2016
[5]	Si based rectangular coupler	70%	2007
[3]	Hybrid linear tapered plasmonic coupler	60-70%	2010
[34]	Wideband plasmonic slot-silicon waveguide couplers	70%	2010
[35]	Nanoplasmonic Air-Slot Coupler	50%	2012
[36]	Symmetrically corrugated Si based plasmonic coupler	73%	2012
[37]	Hybrid metal–insulator plasmonic directional coupler	75%	2013
[4]	Cuprous oxide-based rectangular coupler	56%	2014
[11]	AlAs based rectangular coupler	60%	2015
[11]	Alumina based rectangular coupler	50%	2015
[10]	GLS based rectangular coupler	67%	2014
[38]	Integrated nanoplasmonic air-gap coupler	70%	2014
[39]	Slot-to-slot coupling	73%	2014
[40]	Nano-coupler between MIM and dielectric slab	75%	2018
[8]	Air Slot nano-plasmonic coupler	81%	2020
[41]	Lens funnel coupler	81%	2019
Proposed 1	Simple semi-elliptical	78%	2021
Proposed 2	Air-gap based semi-elliptical	85%	2021

6.2   Future Works

6.2.1   Graded Air Gap based Semi-Elliptical Plasmonic Coupler

Semi-elliptical coupling structure is totally a new concept in the realization of nanoplasmonic couplers. Already, a simple semi-elliptical coupling structure and an air gap-based semi-elliptical coupling structure have been proposed. I have a plan to explore this idea with a graded air gap in between the plasmonic waveguide and dielectric

waveguide. A three-dimensional schematic of the graded air gap-based semi-elliptical nanoplasmonic coupler has been depicted in Section 6.2.1.
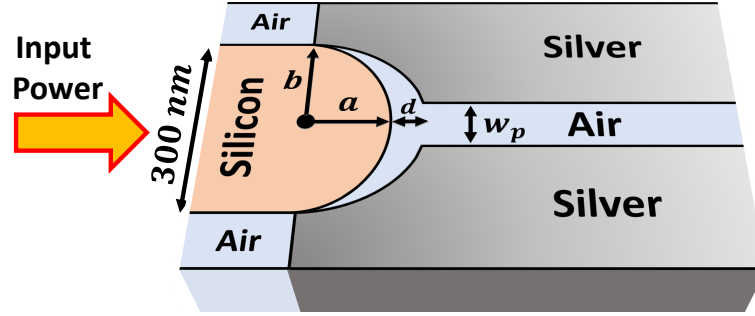
Figure 6.1: Three dimensional view of the proposed graded air gap-based semi-elliptical nano-plasmonic coupler.

Here,

w_p = width of air gap between the metals of the MDM plasmonic waveguide.

a = length of the semi-major axis of the semi-elliptical shape.

b = length of the semi-minor axis of the semi-elliptical shape.

Silicon will be used as the dielectric material of dielectric waveguide. For MDM plasmonic waveguide, silver will be used as the metal and air will be used as the dielectric material.

6.2.2 Possible Potentials of Graded Air Gap-Based Coupler

There are a few expected advantages of the outcomes of the graded air gap-based semi-elliptical nanoplasmonic coupler. They have been mention below:

1. It is expected that the graded air gap-based semi-elliptical nanoplasmonic coupler will have a better coupling efficiency than that of the simple semi-elliptical nanoplasmonic coupler and air gap-based semi-elliptical nanoplasmonic coupler.

2. It will have the capability to tolerate the angular misalignment as well as air gap misalignment between the waveguides. This was was available in the air gap-based semi-elliptical nanoplasmonic coupler mentioned in Chapter 5 but was not available in the simple semi-elliptical nanoplasmonic coupler mentioned in Chapter 4.

3. As this is going to be the offspring of the previous coupler mentioned in Chapters 4 and 5, it's expected that the graded air gap-based semi-elliptical nanoplasmonic coupler will have the ability to operate at a broad range of frequencies.

4. Besides, this coupler is expected to perform better when performance parameters like VSWR, reflectance, absorbance, etc. will be considered.

5. Last but not the least, due to its being simple in structure, the graded air gap-based semi-elliptical nanoplasmonic coupler will be very fabrication friendly.
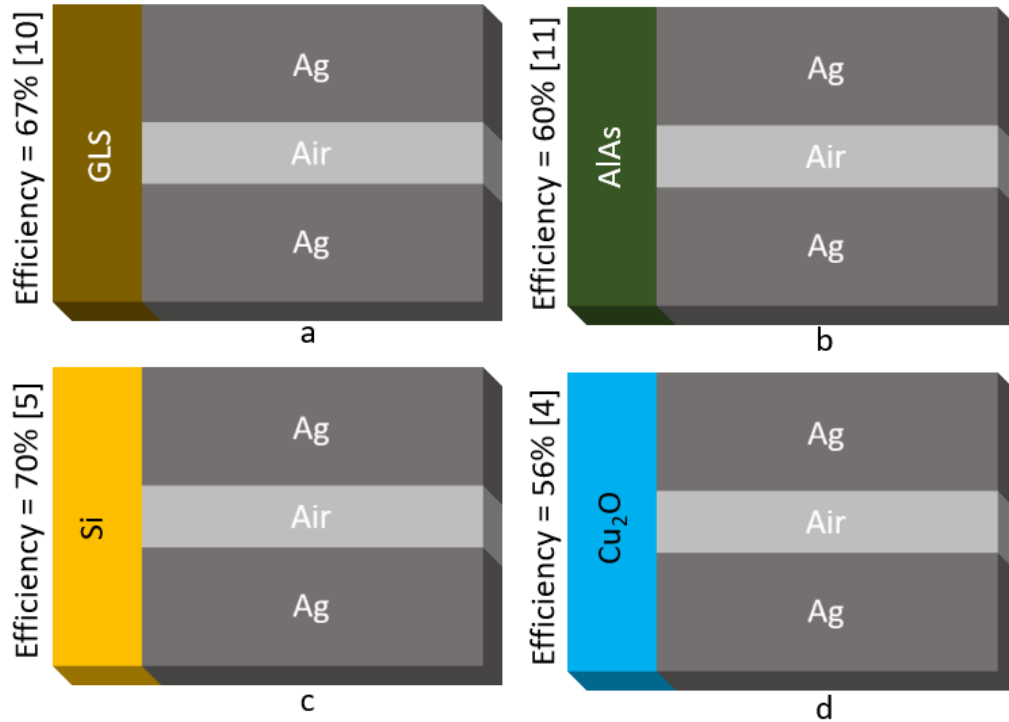
Figure 6.2: Effect of materials on the couplers with same structural features. (a) GLS based rectangular (coupling efficiency of 67%) [10], (b) AlAs based rectangular (coupling efficiency of 60%) [11], (c) Si based rectangular (coupling efficiency of 70%) [5], (d) Cuprous oxide based rectangular (coupling efficiency of 56%) [4]

6.2.3 Impact of Materials on Semi-Elliptical Plasmonic Coupler

Changing materials may give better performance in terms of coupling of the structure. Already, it has been seen from different coupling structures proposed by different researchers, there is a significant impact on the coupling efficiency of the plasmonic couplers based on the materials deployed.

Table 6.2: Variation of performance of rectangular plasmonic couplers based on materials

Ref.	Material	Efficiency %	Year
[5]	Si	70%	2007
[4]	Cuprous oxide	56%	2014

[11]	AlAs	60%	2015
[11]	Alumina	50%	2015
[10]	GLS	67%	2014

As an example, we may consider the rectangular-shaped plasmonic couplers. Where due to the variation of the materials the is a significant change in the performance. A list of the rectangular nanoplasmonic couplers with different performances due to the use of different materials, has been given in Table 6.2. Figure 6.2 shows four couplers where the structure of all of them are same. The only difference between them is the materials used. In Figure 6.2a GLS based rectangular coupler (coupling efficiency of 67%) [10]has been shown. In Figure 6.2b AlAs based rectangular coupler (coupling efficiency of 60%) [11] has been depicted. In Figure 6.2c Si based rectangular coupler (coupling efficiency of 70%) [5] has been shown. In Figure 6.2d Cuprous oxide based rectangular coupler (coupling efficiency of 56%) [4] has been depicted.

In the same way, it's possible to get better results from the semi-elliptical nanoplasmonic couplers. In the upcoming days, this issue can be considered for getting better plasmonic couplers.

Second step photolithography
Silicon deposition

	Substrate
	Photoresist
	Silver

	Mask
	Silicon

First step photolithography
Silver deposition
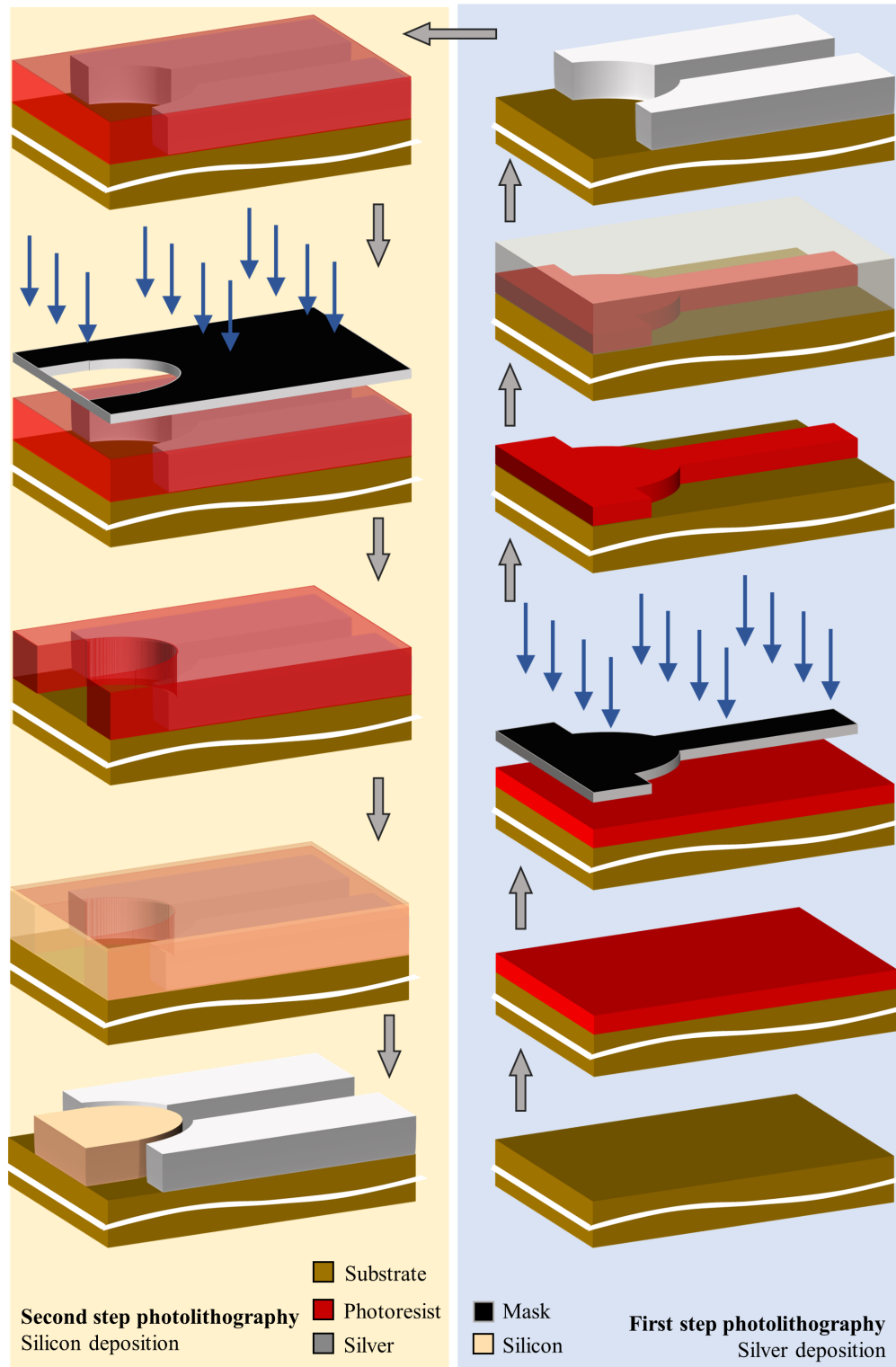
Figure 6.3: Steps to fabricate the proposed couplers.

6.2.4 Fabrication

The most important part of any nano-scale device is the fabrication. By simulation, it's possible to get very efficient, and sophisticated devices but the main challenge is to give the simulated device a physical form. Due to the lack of state-of-the-art growth and fabrication technology, it may be tough to go for the fabrication right now. Thus, fabrication is going to be kept as future work for now. It's possible to go for the fabrication by working in collaboration with some other institutions having the growth and fabrication facilities.

The steps of the fabrication has already been determined. Figure 6.3 will give the detailed idea of how the fabrication process will be completed. Basically, it will have a two step photolithography process. Where, at first the silver will be deposited at the desired location on the substrate. The substrate may be of Si or GaAs. For the silver deposition, Sputtering tool may be used which is actually a physical vapor deposition (PVD) method of thin film deposition. After the deposition of the silver, next photolithography process will take place where silicon will be deposited. Chemical vapor deposition (CVD) process will be used to deposit silicon on the substrate. At the end after the final lift off we will get the fabricated air gap based semi-elliptical nanop plasmonic coupler on the substrate.

List of Publications

CONFERENCE

1. **Md. Saiful Islam Sumon**, Mahir Tazwar, Sakib Mahtab Khondokar, and Rakibul Hasan Sagor, "Design and Analysis of Semi-Elliptical Ultra-Compact Nano-plasmonic Coupler", 2019, 1st International Conference on Robotics, Electrical and Signal Processing Techniques (ICREST), Dhaka, Bangladesh.

2. **Md. Saiful Islam Sumon**, Nowshed Al Nur Hridoy, Anas Mahmood, Rakibul Hasan Sagor, "Designing GaAs Based Semi-Elliptical Nano Plasmonic Coupler with Analytical Assessment", 2020 3rd International Conference on Mechanical, Electronics, Computer, and Industrial Technology (MECnIT), Medan, Indonesia.

3. **Md. Saiful Islam Sumon**, Sheikh Montasir Mahbub, Md. Sami Imtiaz, Rakibul Hasan Sagor, "Air Gap Based Novel Rectangular Nano Plasmonic Coupler Design and Analysis", 2020 IEEE International Conference on Semiconductor Electronics (ICSE), KL, Malaysia

4. **Md. Saiful Islam Sumon**, Md. Omar Sharif, A.B.M Rafid Anwar, Shadman Shahriar Mahmud, Rakibul Hasan Sagor, "Theoretical Investigation of a GaAs Based Novel Air Slot Nano-Plasmonic Coupler", 2020 IEEE Region 10 Symposium (TENSYMP), 5-7 June 2020, Dhaka, Bangladesh.

5. Md. Farhad Hassan; **Md. Saiful Islam Sumon**; Md. Moudud Hasan; Md. Arefin Rabbi Emon; Rakibul Hasan Sagor, "Design and Analysis of a Highly Efficient Rectangular Cavity Based Semi-Elliptic Nanoplasmonic Coupler", 2020 IEEE 8th R10 Humanitarian Technology Conference (R10-HTC), Sarawak, Malaysia.

JOURNAL

1. Rakibul Hasan Sagor, **Md. Saiful Islam Sumon**, Mahir Tazwar, "Design and Analysis of a Novel Air Gap Based Semi-Elliptical Nano-plasmonic Coupler", Plasmonics, 2019

2. Syed M. N. Hasan, Weicheng You, **Md Saiful Islam Sumon** , and Shamsul Arafin, "Recent Progress of Electrically Pumped AlGaN Diode Lasers in the UV-B and -C Bands", Photonics 2021, 8(7), 267

REFERENCES

[1] J. Zhang, L. Zhang, and W. Xu, "Surface plasmon polaritons: physics and applications," *Journal of Physics D: Applied Physics*, vol. 45, no. 11, p. 113001, 2012.

[2] D. K. Gramotnev and S. I. Bozhevolnyi, "Plasmonics beyond the diffraction limit," *Nature photonics*, vol. 4, no. 2, pp. 83–91, 2010.

[3] Y. Song, J. Wang, Q. Li, M. Yan, and M. Qiu, "Broadband coupler between silicon waveguide and hybrid plasmonic waveguide," *Optics express*, vol. 18, no. 12, pp. 13 173–13 179, 2010.

[4] Saber, Md Ghulam and Sagor, Rakibul Hasan, "Analysis of cuprous oxide-based ultra-compact nanoplasmonic coupler," *Applied Nanoscience*, vol. 5, no. 2, pp. 217–221, 2015.

[5] G. Veronis and S. Fan, "Theoretical investigation of compact couplers between dielectric slab waveguides and two-dimensional metal-dielectric-metal plasmonic waveguides," *Optics Express*, vol. 15, no. 3, pp. 1211–1221, 2007.

[6] R. A. Wahsheh, Z. Lu, and M. A. Abushagur, "Nanoplasmonic couplers and splitters," *Optics Express*, vol. 17, no. 21, pp. 19 033–19 040, 2009.

[7] P. Ginzburg and M. Orenstein, "Plasmonic transmission lines: from micro to nano scale with $\lambda/4$ impedance matching," *Optics express*, vol. 15, no. 11, pp. 6762–6767, 2007.

[8] M. S. I. Sumon, M. O. Sharif, A. R. Anwar, S. S. Mahmud, and R. H. Sagor, "Theoretical investigation of a GaAs based novel air slot nano-plasmonic coupler," in *2020 IEEE Region 10 Symposium (TENSYMP).* IEEE, 2020, pp. 1123–1127.

[9] R. A. Wahsheh and M. A. Abushagur, "Experimental and theoretical investigations of an air-slot coupler between dielectric and plasmonic waveguides," *Optics express*, vol. 24, no. 8, pp. 8237–8242, 2016.

[10] Saber, Md Ghulam and Sagor, Rakibul Hasan, "Design and analysis of a gallium lanthanum sulfide based nanoplasmonic coupler yielding 67% efficiency."

[11] Saber, Md Ghulam and Sagor, Rakibul Hasan, "Design and study of nano-plasmonic couplers using aluminium arsenide and alumina," *IET Optoelectronics*, vol. 9, no. 3, pp. 125–130, 2015.

[12] E. D. Palik, *Handbook of optical constants of solids*. Academic press, 1998, vol. 3.

[13] W. L. Barnes, A. Dereux, and T. W. Ebbesen, "Surface plasmon subwavelength optics," *nature*, vol. 424, no. 6950, pp. 824–830, 2003.

[14] S. I. Bozhevolnyi, J. Erland, K. Leosson, P. M. Skovgaard, and J. M. Hvam, "Waveguiding in surface plasmon polariton band gap structures," *Physical review letters*, vol. 86, no. 14, p. 3008, 2001.

[15] J. Homola, S. S. Yee, and G. Gauglitz, "Surface plasmon resonance sensors," *Sensors and actuators B: Chemical*, vol. 54, no. 1-2, pp. 3–15, 1999.

[16] G. Raschke, S. Brogl, A. Susha, A. Rogach, T. Klar, J. Feldmann, B. Fieres, N. Petkov, T. Bein, A. Nichtl *et al.*, "Gold nanoshells improve single nanoparticle molecular sensors," *Nano letters*, vol. 4, no. 10, pp. 1853–1857, 2004.

[17] J. Homola, "Present and future of surface plasmon resonance biosensors," *Analytical and bioanalytical chemistry*, vol. 377, no. 3, pp. 528–539, 2003.

[18] D. G. Georganopoulou, L. Chang, J.-M. Nam, C. S. Thaxton, E. J. Mufson, W. L. Klein, and C. A. Mirkin, "Nanoparticle-based detection in cerebral spinal fluid of a soluble pathogenic biomarker for alzheimer's disease," *Proceedings of the National Academy of Sciences*, vol. 102, no. 7, pp. 2273–2276, 2005.

[19] K. Kneipp, Y. Wang, H. Kneipp, L. T. Perelman, I. Itzkan, R. R. Dasari, and M. S. Feld, "Single molecule detection using surface-enhanced raman scattering (sers)," *Physical review letters*, vol. 78, no. 9, p. 1667, 1997.

[20] A. M. Michaels, M. Nirmal, and L. Brus, "Surface enhanced raman spectroscopy of individual rhodamine 6g molecules on large ag nanocrystals," *Journal of the American Chemical Society*, vol. 121, no. 43, pp. 9932–9939, 1999.

[21] Y. Fang, H. Wei, F. Hao, P. Nordlander, and H. Xu, "Remote-excitation surface-enhanced raman scattering using propagating ag nanowire plasmons," *Nano letters*, vol. 9, no. 5, pp. 2049–2053, 2009.

[22] P. Zijlstra, J. W. Chon, and M. Gu, "Five-dimensional optical recording mediated by surface plasmons in gold nanorods," *nature*, vol. 459, no. 7245, pp. 410–413, 2009.

[23] C. Hermann, V. Kosobukin, G. Lampel, J. Peretti, V. Safarov, and P. Bertrand, "Surface-enhanced magneto-optics in metallic multilayer films," *Physical Review B*, vol. 64, no. 23, p. 235422, 2001.

[24] M. Westphalen, U. Kreibig, J. Rostalski, H. Lüth, and D. Meissner, "Metal cluster enhanced organic solar cells," *Solar energy materials and solar cells*, vol. 61, no. 1, pp. 97–105, 2000.

[25] V. E. Ferry, L. A. Sweatlock, D. Pacifici, and H. A. Atwater, "Plasmonic nanostructure design for efficient light coupling into solar cells," *Nano letters*, vol. 8, no. 12, pp. 4391–4397, 2008.

[26] H. J. Lezec, A. Degiron, E. Devaux, R. Linke, L. Martin-Moreno, F. Garcia-Vidal, and T. Ebbesen, "Beaming light from a subwavelength aperture," *science*, vol. 297, no. 5582, pp. 820–822, 2002.

[27] G. Lerosey, D. Pile, P. Matheu, G. Bartal, and X. Zhang, "Controlling the phase and amplitude of plasmon sources at a subwavelength scale," *Nano letters*, vol. 9, no. 1, pp. 327–331, 2009.

[28] S. Maier, P. Kik, and H. Atwater, "a, meltzer, s., harel, e., koel, be, requicha, aag," *Nat. Mater*, vol. 2, pp. 229–232, 2003.

[29] R. F. Oulton, V. J. Sorger, D. Genov, D. Pile, and X. Zhang, "A hybrid plasmonic waveguide for subwavelength confinement and long-range propagation," *nature photonics*, vol. 2, no. 8, p. 496, 2008.

[30] Z. Han, A. Elezzabi, and V. Van, "Experimental realization of subwavelength plasmonic slot waveguides on a silicon platform," *Optics letters*, vol. 35, no. 4, pp. 502–504, 2010.

[31] R. A. Wahsheh, Z. Lu, and M. A. Abushagur, "Experimental investigation of a nanoplasmonic air-slot coupler toward dense optical integrated circuits," in *Frontiers in Optics*. Optical Society of America, 2015, pp. FW3E–2.

[32] R. Yang, R. A. Wahsheh, Z. Lu, and M. A. Abushagur, "Efficient light coupling between dielectric slot waveguide and plasmonic slot waveguide," *Optics letters*, vol. 35, no. 5, pp. 649–651, 2010.

[33] B. Q. Zhu and H. K. Tsang, "High coupling efficiency silicon waveguide to metal–insulator–metal waveguide mode converter," *Journal of Lightwave Technology*, vol. 34, no. 10, pp. 2467–2472, 2016.

[34] B. Lau, M. A. Swillam, and A. S. Helmy, "Hybrid orthogonal junctions: wideband plasmonic slot-silicon waveguide couplers," *Optics express*, vol. 18, no. 26, pp. 27 048–27 059, 2010.

[35] R. A. Wahsheh, Z. Lu, and M. A. Abushagur, "Nanoplasmonic air-slot coupler: design and fabrication," in *Frontiers in optics*. Optical Society of America, 2012, pp. FTh4A–6.

[36] R. Thomas, Z. Ikonic, and R. Kelsall, "Silicon based plasmonic coupler," *Optics express*, vol. 20, no. 19, pp. 21 520–21 531, 2012.

[37] M. T. Noghani and M. H. V. Samiei, "Ultrashort hybrid metal–insulator plasmonic directional coupler," *Applied optics*, vol. 52, no. 31, pp. 7498–7503, 2013.

[38] R. A. Wahsheh, Z. Lu, and M. A. Abushagur, "Ultra-compact integrated nanoplasmonic air-gap coupler," in *Frontiers in Optics*. Optical Society of America, 2014, pp. FTh4E–5.

[39] D. Kong and M. Tsubokawa, "Evaluation of slot-to-slot coupling between dielectric slot waveguides and metal-insulator-metal slot waveguides," *Optics express*, vol. 23, no. 15, pp. 19 082–19 091, 2015.

[40] M. B. Heydari, M. Asgari, and N. Jafari, "Novel analytical model for nanocoupler between metal–insulator–metal plasmonic and dielectric slab waveguides," *Optical and Quantum Electronics*, vol. 50, no. 12, pp. 1–11, 2018.

[41] S. H. Badri and M. Gilarlue, "Coupling between silicon waveguide and metal-dielectric-metal plasmonic waveguide with lens-funnel structure," *Plasmonics*, pp. 1–7, 2019.

[42] A. D. Rakić, A. B. Djurišić, J. M. Elazar, and M. L. Majewski, "Optical properties of metallic films for vertical-cavity optoelectronic devices," *Applied optics*, vol. 37, no. 22, pp. 5271–5283, 1998.

[43] Z. L. Sámson, S.-C. Yen, K. F. MacDonald, K. Knight, S. Li, D. W. Hewak, D.-P. Tsai, and N. I. Zheludev, "Chalcogenide glasses in active plasmonics," *physica status solidi (RRL)–Rapid Research Letters*, vol. 4, no. 10, pp. 274–276, 2010.

[44] E. Ozbay, "Plasmonics: merging photonics and electronics at nanoscale dimensions," *science*, vol. 311, no. 5758, pp. 189–193, 2006.

[45] S. Kawata, Y. Inouye, and P. Verma, "Plasmonics for near-field nano-imaging and superlensing," *Nature photonics*, vol. 3, no. 7, pp. 388–394, 2009.

[46] W. Adams, A. Ghoshroy, and D. O. Guney, "Plasmonic superlens imaging enhanced by incoherent active convolved illumination," *ACS Photonics*, vol. 5, no. 4, pp. 1294–1302, 2018.

[47] H. Li, L. Fu, K. Frenner, and W. Osten, "Cascaded plasmonic superlens for far-field imaging with magnification at visible wavelength," *Optics express*, vol. 26, no. 8, pp. 10 888–10 897, 2018.

[48] M. Fehrenbacher, S. Winnerl, H. Schneider, J. Dooring, S. C. Kehr, L. M. Eng, Y. Huo, O. G. Schmidt, K. Yao, Y. Liu *et al.*, "Plasmonic superlensing in doped GaAs," *Nano letters*, vol. 15, no. 2, pp. 1057–1061, 2015.

[49] K. A. Willets and R. P. Van Duyne, "Localized surface plasmon resonance spectroscopy and sensing," *Annu. Rev. Phys. Chem.*, vol. 58, pp. 267–297, 2007.

[50] Z. Jakšic, O. Jakšic, and J. Matovic, "Performance limits to the operation of nanoplasmonic chemical sensors: noise-equivalent refractive index and detectivity," *Journal of Nanophotonics*, vol. 3, no. 1, p. 031770, 2009.

[51] M. E. Stewart, C. R. Anderton, L. B. Thompson, J. Maria, S. K. Gray, J. A. Rogers, and R. G. Nuzzo, "Nanostructured plasmonic sensors," *Chemical reviews*, vol. 108, no. 2, pp. 494–521, 2008.

[52] A. V. Kabashin, P. Evans, S. Pastkovsky, W. Hendren, G. A. Wurtz, R. Atkinson, R. Pollard, V. Podolskiy, and A. V. Zayats, "Plasmonic nanorod metamaterials for biosensing," *Nature materials*, vol. 8, no. 11, pp. 867–871, 2009.

[53] K. Catchpole, , and A. Polman, "Plasmonic solar cells," *Optics express*, vol. 16, no. 26, pp. 21 793–21 800, 2008.

[54] Y. H. Jang, Y. J. Jang, S. Kim, L. N. Quan, K. Chung, and D. H. Kim, "Plasmonic solar cells: from rational design to mechanism overview," *Chemical reviews*, vol. 116, no. 24, pp. 14 982–15 034, 2016.

[55] K. Ueno, T. Oshikiri, Q. Sun, X. Shi, and H. Misawa, "Solid-state plasmonic solar cells," *Chemical reviews*, vol. 118, no. 6, pp. 2955–2993, 2017.

[56] S. D. Standridge, G. C. Schatz, and J. T. Hupp, "Toward plasmonic solar cells: protection of silver nanoparticles via atomic layer deposition of tio2," *Langmuir*, vol. 25, no. 5, pp. 2596–2600, 2009.

[57] J. Henzie, M. H. Lee, and T. W. Odom, "Multiscale patterning of plasmonic metamaterials," *Nature nanotechnology*, vol. 2, no. 9, pp. 549–554, 2007.

[58] F. Garcia-Vidal, L. Martin-Moreno, and J. Pendry, "Surfaces with holes in them: new plasmonic metamaterials," *Journal of optics A: Pure and applied optics*, vol. 7, no. 2, p. S97, 2005.

[59] A. Boltasseva and H. A. Atwater, "Low-loss plasmonic metamaterials," *Science*, vol. 331, no. 6015, pp. 290–291, 2011.

[60] K. Yao and Y. Liu, "Plasmonic metamaterials," *Nanotechnology Reviews*, vol. 3, no. 2, pp. 177–210, 2014.

[61] K. K. Madapu, A. K. Sivadasan, M. Baral, and S. Dhara, "Observation of surface plasmon polaritons in 2d electron gas of surface electron accumulation in inn nanostructures," *Nanotechnology*, vol. 29, no. 27, p. 275707, 2018.

[62] X. Zhang and J. Yang, "Ultrafast plasmonic optical switching structures and devices," *Frontiers in Physics*, vol. 7, p. 190, 2019.

[63] S. A. Maier, "Plasmonics: The promise of highly integrated optical devices," *IEEE Journal of selected topics in Quantum Electronics*, vol. 12, no. 6, pp. 1671–1677, 2006.

[64] S. A. Maier, M. L. Brongersma, P. G. Kik, S. Meltzer, A. A. Requicha, and H. A. Atwater, "Plasmonics—a route to nanoscale optical devices," *Advanced materials*, vol. 13, no. 19, pp. 1501–1505, 2001.

[65] P. G. Kik, S. A. Maier, and H. A. Atwater, "Plasmon printing–a new approach to near-field lithography," *MRS Online Proceedings Library (OPL)*, vol. 705, 2001.

[66] H. B. Lu, J. Homola, C. T. Campbell, G. G. Nenninger, S. S. Yee, and B. D. Ratner, "Protein contact printing for a surface plasmon resonance biosensor with on-chip referencing," *Sensors and Actuators B: Chemical*, vol. 74, no. 1-3, pp. 91–99, 2001.

[67] S. Natarajan, P. S. Katsamba, A. Miles, J. Eckman, G. A. Papalia, R. L. Rich, B. K. Gale, and D. G. Myszka, "Continuous-flow microfluidic printing of proteins for array-based applications including surface plasmon resonance imaging," *Analytical Biochemistry*, vol. 373, no. 1, pp. 141–146, 2008.

[68] Y. Jin and X. Gao, "Plasmonic fluorescent quantum dots," *Nature nanotechnology*, vol. 4, no. 9, pp. 571–576, 2009.

[69] O. Bitton, S. N. Gupta, and G. Haran, "Quantum dot plasmonics: from weak to strong coupling," *Nanophotonics*, vol. 8, no. 4, pp. 559–575, 2019.

[70] J. Ho, J. Tatebayashi, S. Sergent, C. F. Fong, Y. Ota, S. Iwamoto, and Y. Arakawa, "A nanowire-based plasmonic quantum dot laser," *Nano letters*, vol. 16, no. 4, pp. 2845–2850, 2016.

[71] T. A. Larson, J. Bankson, J. Aaron, and K. Sokolov, "Hybrid plasmonic magnetic nanoparticles as molecular specific agents for mri/optical imaging and photothermal therapy of cancer cells," *Nanotechnology*, vol. 18, no. 32, p. 325101, 2007.

[72] J. Z. Zhang, "Biomedical applications of shape-controlled plasmonic nanostructures: a case study of hollow gold nanospheres for photothermal ablation ther-

apy of cancer," *The Journal of Physical Chemistry Letters*, vol. 1, no. 4, pp. 686–695, 2010.

[73] Y. T. Lim, M. Y. Cho, J. K. Kim, S. Hwangbo, and B. H. Chung, "Plasmonic magnetic nanostructure for bimodal imaging and photonic-based therapy of cancer cells," *ChemBioChem*, vol. 8, no. 18, pp. 2204–2209, 2007.

[74] X. Huang, P. K. Jain, I. H. El-Sayed, and M. A. El-Sayed, "Plasmonic photothermal therapy (pptt) using gold nanoparticles," *Lasers in medical science*, vol. 23, no. 3, pp. 217–228, 2008.

[75] A. N. Grigorenko, M. Polini, and K. Novoselov, "Graphene plasmonics," *Nature photonics*, vol. 6, no. 11, pp. 749–758, 2012.

[76] F. J. Garcia de Abajo, "Graphene plasmonics: challenges and opportunities," *Acs Photonics*, vol. 1, no. 3, pp. 135–152, 2014.

[77] P. A. D. Gonçalves and N. M. Peres, *An introduction to graphene plasmonics*. World Scientific, 2016.

[78] A. Alù and N. Engheta, "Multifrequency optical invisibility cloak with layered plasmonic shells," *Physical review letters*, vol. 100, no. 11, p. 113901, 2008.

[79] J. Renger, M. Kadic, G. Dupont, S. S. Aćimović, S. Guenneau, R. Quidant, and S. Enoch, "Hidden progress: broadband plasmonic invisibility," *Optics Express*, vol. 18, no. 15, pp. 15 757–15 768, 2010.

[80] W. Kort-Kamp, F. Rosa, F. Pinheiro, and C. Farina, "Tuning plasmonic cloaks with an external magnetic field," *Physical review letters*, vol. 111, no. 21, p. 215504, 2013.

[81] J. Takahara, S. Yamagishi, H. Taki, A. Morimoto, and T. Kobayashi, "Guiding of a one-dimensional optical beam with nanometer diameter," *Optics letters*, vol. 22, no. 7, pp. 475–477, 1997.

[82] S. A. Maier, P. E. Barclay, T. J. Johnson, M. D. Friedman, and O. Painter, "Low-loss fiber accessible plasmon waveguide for planar energy guiding and sensing," *Applied Physics Letters*, vol. 84, no. 20, pp. 3990–3992, 2004.

[83] S. A. Maier, M. D. Friedman, P. E. Barclay, and O. Painter, "Experimental demonstration of fiber-accessible metal nanoparticle plasmon waveguides for planar energy guiding and sensing," *Applied Physics Letters*, vol. 86, no. 7, p. 071103, 2005.

[84] S. A. Maier, P. G. Kik, H. A. Atwater, S. Meltzer, E. Harel, B. E. Koel, and A. A. Requicha, "Local detection of electromagnetic energy transport below the diffraction limit in metal nanoparticle plasmon waveguides," *Nature materials*, vol. 2, no. 4, pp. 229–232, 2003.

[85] L. Chen, J. Shakya, and M. Lipson, "Subwavelength confinement in an integrated metal slot waveguide on silicon," *Optics letters*, vol. 31, no. 14, pp. 2133–2135, 2006.

[86] R. F. Oulton, V. J. Sorger, D. Genov, D. Pile, and X. Zhang, "A hybrid plasmonic waveguide for subwavelength confinement and long-range propagation," *nature photonics*, vol. 2, no. 8, p. 496, 2008.

[87] R. Oulton, G. Bartal, D. Pile, and X. Zhang, "Confinement and propagation characteristics of subwavelength plasmonic modes," *New Journal of Physics*, vol. 10, no. 10, p. 105018, 2008.

[88] H. Li, J. W. Noh, Y. Chen, and M. Li, "Enhanced optical forces in integrated hybrid plasmonic waveguides," *Optics express*, vol. 21, no. 10, pp. 11 839–11 851, 2013.

[89] X. Yang, Y. Liu, R. F. Oulton, X. Yin, and X. Zhang, "Optical forces in hybrid plasmonic waveguides," *nano Letters*, vol. 11, no. 2, pp. 321–328, 2011.

[90] J.-C. Weeber, A. Dereux, C. Girard, J. R. Krenn, and J.-P. Goudonnet, "Plasmon polaritons of metallic nanowires for controlling submicron propagation of light," *Physical Review B*, vol. 60, no. 12, p. 9061, 1999.

[91] A. Sivadasan, M. Sardar, and S. Dhara, "Far field photoluminescence imaging of single algan nanowire in the sub-wavelength scale using confinement of polarized light," *Annalen der Physik*, vol. 529, no. 3, p. 1600165, 2017.

[92] B. Steinberger, A. Hohenau, H. Ditlbacher, A. Stepanov, A. Drezet, F. Aussenegg, A. Leitner, and J. Krenn, "Dielectric stripes on gold as surface plasmon waveguides," *Applied Physics Letters*, vol. 88, no. 9, p. 094104, 2006.

[93] N. Fang, H. Lee, C. Sun, and X. Zhang, "Sub–diffraction-limited optical imaging with a silver superlens," *Science*, vol. 308, no. 5721, pp. 534–537, 2005.

[94] J. Rho, Z. Ye, Y. Xiong, X. Yin, Z. Liu, H. Choi, G. Bartal, and X. Zhang, "Spherical hyperlens for two-dimensional sub-diffractional imaging at visible frequencies," *Nature communications*, vol. 1, no. 1, pp. 1–5, 2010.

[95] S. I. Bozhevolnyi, V. S. Volkov, E. Devaux, and T. W. Ebbesen, "Channel plasmon-polariton guiding by subwavelength metal grooves," *Physical review letters*, vol. 95, no. 4, p. 046802, 2005.

[96] J.-C. Weeber, Y. Lacroute, A. Dereux, E. Devaux, T. Ebbesen, C. Girard, M. U. González, and A.-L. Baudrion, "Near-field characterization of bragg mirrors engraved in surface plasmon waveguides," *Physical Review B*, vol. 70, no. 23, p. 235406, 2004.

[97] M. S. I. Sumon, M. Tazwar, R. H. Sagor, and S. M. Khandaker, "Design and analysis of a semi-elliptical ultra-compact nano-plasmonic coupler," in *2019 International Conference on Robotics, Electrical and Signal Processing Techniques (ICREST)*. IEEE, 2019, pp. 417–421.

[98] D. Pile and D. Gramotnev, "Adiabatic and nonadiabatic nanofocusing of plasmons by tapered gap plasmon waveguides," *Applied Physics Letters*, vol. 89, no. 4, p. 041111, 2006.

[99] E. Wadbro and C. Engström, "Topology and shape optimization of plasmonic nano-antennas," *Computer Methods in Applied Mechanics and Engineering*, vol. 293, pp. 155–169, 2015.

[100] Y. Deng, Z. Liu, C. Song, J. Wu, Y. Liu, and Y. Wu, "Topology optimization-based computational design methodology for surface plasmon polaritons," *Plasmonics*, vol. 10, no. 3, pp. 569–583, 2015.

[101] J. Andkjær, S. Nishiwaki, T. Nomura, and O. Sigmund, "Topology optimization of grating couplers for the efficient excitation of surface plasmons," *JOSA B*, vol. 27, no. 9, pp. 1828–1832, 2010.

[102] T. Weiland, "A discretization model for the solution of maxwell's equations for six-component fields," *Archiv Elektronik und Uebertragungstechnik*, vol. 31, pp. 116–120, 1977.

[103] M. Clemens and T. Weiland, "Magnetic field simulation using conformal fit formulations," *IEEE transactions on magnetics*, vol. 38, no. 2, pp. 389–392, 2002.

[104] K. Yee, "Numerical solution of initial boundary value problems involving maxwell's equations in isotropic media," *IEEE Transactions on antennas and propagation*, vol. 14, no. 3, pp. 302–307, 1966.

[105] R. Marklein, *The finite integration technique as a general tool to compute acoustic, electromagnetic, elastodynamic, and coupled wave fields*. IEEE Press and John Wiley and Sons, New York, NY, USA, 2002.

[106] S. M. Rao, G. K. Gothard, and D. R. Wilton, "Application of finite-integral technique to electromagnetic scattering by two-dimensional cavity-backed aperture in a ground plane," *IEEE Transactions on Antennas and Propagation*, vol. 46, no. 5, pp. 679–685, 1998.

[107] K. Langenberg, M. Brandfaß, R. Hannemann, T. Kaczorowski, J. Kostka, C. Hofmann, R. Marklein, K. Mayer, and A. Pitsch, "Inverse scattering with acoustic, electromagnetic, and elastic waves as applied in nondesctructive evaluation," in *Wavefield inversion*. Springer, 1999, pp. 59–118.

[108] M. Funieru, H. De Gersem, and T. Weiland, "Transient simulation of a linear actuator discretized by the finite integration technique," in *Scientific Computing in Electrical Engineering*.   Springer, 2007, pp. 281–286.

[109] I. Munteanu and T. Weiland, "Rf & microwave simulation with the finite integration technique–from component to system design," in *Scientific Computing in Electrical Engineering*.   Springer, 2007, pp. 247–260.

[110] S. Chew, M. Leong, and P. Kooi, "Application of the finite integration technique to the problem of whispering-gallery modes," *Electronics Letters*, vol. 29, no. 10, pp. 888–890, 1993.

[111] V. Motrescu and U. Rienen, "Simulation of electromagnetic ftelds in the human body using finite integration technique (fit)," 2002.

[112] S. Gutschling, H. Krüger, and T. Weiland, "Time-domain simulation of dispersive media with the finite integration technique," *International Journal of Numerical Modelling: Electronic Networks, Devices and Fields*, vol. 13, no. 4, pp. 329–348, 2000.

[113] C. Haase and H. Stiebig, "Thin-film silicon solar cells with efficient periodic light trapping texture," *Applied physics letters*, vol. 91, no. 6, p. 061116, 2007.

[114] J.-P. Berenger, "A perfectly matched layer for the absorption of electromagnetic waves," *Journal of computational physics*, vol. 114, no. 2, pp. 185–200, 1994.

[115] A. Al Noor, M. T. Al-Amin, R. H. Sagor, and M. G. Saber, "Guiding surface plasmon polariton along 90 degree bend mdm waveguide models," in *Advances in Electrical Engineering (ICAEE), 2013 International Conference on*.   IEEE, 2013, pp. 124–128.

[116] M. G. Saber and R. H. Sagor, "A comparative study of dielectric materials as nano-plasmonic couplers," in *Electrical Engineering Congress (iEECON), 2014 International*.   IEEE, 2014, pp. 1–4.

[117] Md. Ghulam Saber and Rakibul Hasan Sagor, "Analysis of cuprous oxide-based ultra-compact nanoplasmonic coupler," *Applied Nanoscience*, vol. 5, no. 2, pp. 217–221, apr 2014. [Online]. Available: https: //doi.org/10.1007%2Fs13204-014-0308-3

[118] Md. Ghulam Saber and Rakibul Hasan Sagor, "Design and study of nano-plasmonic couplers using aluminium arsenide and alumina," *IET Optoelectronics*, vol. 9, no. 3, pp. 125–130, jun 2015. [Online]. Available: https://doi.org/10.1049%2Fiet-opt.2014.0027

[119] A. Boltasseva, K. Leosson, T. Rosenzveig, R. B. Nielsen, R. H. Pedersen, K. B. Jørgensen, I. Fernandez-Cuesta, J. Jung, T. Søndergaard, S. I.

Bozhevolnyi, and A. Kristensen, "Fabrication of plasmonic waveguides for device applications," in *Photonic Metamaterials*, M. A. Noginov, N. I. Zheludev, A. D. Boardman, and N. Engheta, Eds.   SPIE, sep 2007. [Online]. Available: https://doi.org/10.1117%2F12.732836